Available online at www.sciencedirect.com

ScienceDirect

Geochimica et Cosmochimica Acta 320 (2022) 279–303

Geochimica et Cosmochimica Acta

www.elsevier.com/locate/gca

Applications of Pb isotopes in granite K-feldspar and Pb evolution in the Yilgarn Craton

Andreas Zametzer [a,*], Christopher L. Kirkland [a], Michael I.H. Hartnady [a], Milo Barham [a], David C. Champion [b], Simon Bodorkos [b], R. Hugh Smithies [c,a], Simon P. Johnson [c]

[a] *Timescales of Mineral Systems Group, The Institute for Geoscience Research (TIGeR), School of Earth and Planetary Sciences, Curtin University, GPO Box U1987, Perth, WA 6845, Australia*

[b] *Geoscience Australia, GPO Box 378, Canberra, ACT 2601, Australia*

[c] *Geological Survey of Western Australia, Department of Mines, Industry Regulation and Safety, Mineral House, 100 Plain Street, East Perth, WA 6004, Australia*

Received 6 August 2021; accepted in revised form 26 November 2021; Available online 3 December 2021

Abstract

The isotopic composition of Pb in a mineral or rock at the moment it formed – often referred to as common Pb – provides an important tool to track geological processes through time and space. There is a wide range of applications of common Pb isotopes including understanding magma sources, melt production, fractionation, contamination, and crystallization in the crust. Pb but not U is incorporated into the structure of K-feldspar during crystal growth, which, together with its widespread occurrence as a framework mineral, makes it an excellent common Pb tracer. Consequently, common Pb isotopes in granite K-feldspar crystals provide a potential signature of source composition and a link to crustal growth processes in the mid to lower crust. Hence, combining common Pb isotopes with Sm-Nd (or Lu-Hf) isotopic signatures from the same dated rocks allows assessment of the degree of isotopic communication from deep fractionation systems to those higher in the crustal column. In this contribution, we analyze common Pb isotopic signatures in K-feldspar from a granite sample transect through the Archean Yilgarn Craton in Western Australia. This transect crosses the major crustal-scale Ida Fault that is apparent on Nd and Hf isotopic maps and interpreted as a fundamental lithospheric boundary across which magma sources change. Our results yield a difference in median values of the Pb isotope derivative parameters μ ($^{238}U/^{204}Pb$) and ω ($^{232}Th/^{204}Pb$) across the Ida Fault, with higher μ and ω associated with more evolved Nd and Hf isotopic signatures on the western side of the fault. Pb evolution in the Yilgarn Craton is distinct from the widely applied Stacey & Kramers (1975) model. New Yilgarn-specific Pb evolution models are developed with implication for common Pb correction. A correlation in the spatial trends of granite K-feldspar common Pb signatures with those of upper crustal Pb ores and also the Sm-Nd and Lu-Hf systems reveals geochemical communication all the way through the crustal column, implying a common source for the entire lithospheric section on each side of the Ida Fault. Pb isotopes in granite K-feldspar are not an independent geochronometer but may yield important source context on major phase silicate growth that helps refine U-Pb geochronology interpretations (e.g., distinguishing magmatic versus metamorphic zircon growth).

Keywords: Common Pb; Crustal evolution; Yilgarn Craton; Feldspar; Granite; Magma source

* Corresponding author.
E-mail address: andreas.zametzer@postgrad.curtin.edu.au (A. Zametzer).

https://doi.org/10.1016/j.gca.2021.11.029

1. INTRODUCTION

Earth's continental crust is heterogeneous. This heterogeneity reflects a variety of geological processes including magmatic fractionation, magma-mixing, mingling, hybridization (crust-mantle interaction), and variable assimilation (crustal reworking) throughout Earth's history. Unravelling the relative importance of these processes is fundamental in tracking both the evolution of the planetary lithosphere, as well as the spatial distribution of mineral systems within it (e.g., Champion & Sheraton, 1997; Champion, 2013; Champion & Huston, 2016; Blichert-Toft et al., 2016). Traditionally, isotopes of the radiogenic decay systems Sm-Nd and Lu-Hf have been used to image crustal composition in both space and time (Cassidy & Champion, 2004; Champion & Cassidy, 2007; Mole et al., 2014, 2019). However, common Pb isotopes offer a somewhat underutilized, but potentially powerful, additional approach in tracking a range of geological processes through deep time (Gariépy & Allègre, 1985; Halla, 2018).

Initial or common Pb is defined as any Pb incorporated into a crystal or rock at the time of formation. Unlike radiogenic Pb signatures that stem from closed system, in situ radioactive decay of U or Th parent isotopes, common Pb signatures reflect the primary Pb composition of the source at crystallization. The common Pb isotopic ratio is a product of the U-Th-Pb fractionation history of the source material. Accordingly, common Pb isotopic ratios reveal the relative U or Th content (U/Pb or Th/Pb ratio) of the source magma from which a mineral grew; hence, Pb isotopes provide valuable information that aids understanding of crust-mantle differentiation processes. As U and Th are lithophile elements and strongly fractionate into the melt during partial melting of the mantle (Pb is enriched in the crust), this isotope system may trace planetary differentiation and act as a powerful source-tracking tool (e.g., Zartman & Wasserburg, 1969; Gancarz & Wasserburg, 1977; Koeppel & Gruenenfelder, 1979; Blichert-Toft et al., 2016; Halla, 2018).

On a regional scale, Pb isotopes provide a means to understand crustal structure, as melt generation, fractionation, melt contamination, or a combination of these processes may lead to Pb mixing, which will produce distinctive U/Pb or Th/Pb ratios that can be isotopically traced in derivative melts (e.g., Zartman & Wasserburg, 1969; Blaxland et al., 1979; Gariépy & Allègre, 1985; Wareham et al., 1998). On the continental scale, Pb isotopes can potentially be used to help delineate crustal boundaries (plate boundaries or terrane boundaries) separating major lithotectonic blocks with coherent crustal growth histories (e.g., Zartman, 1974; Carignan et al., 1993; Wooden et al., 1998; Wareham et al., 1998; Halla, 2014). Pb isotopes also contribute to tracing orogenic systems through time (e.g., Blichert-Toft et al., 2016; Arcuri & Dickin, 2018). Furthermore, Pb isotopes may help in identifying metamorphic events, determining likely metamorphic ages, and assessing tectonic models for specific regions (e.g., Gancarz & Wasserburg, 1977; Gariépy et al., 1990; Halla, 2005). This range of applications, together with the fact that Pb is frequently bound in ore systems and that original ratios are preserved in the Pb ore galena (PbS), has proven useful in investigating the source, timing and duration of hydrothermal fluid flow and mineralization in many metal deposits (e.g., Doe & Stacey, 1974; Browning et al., 1987; Huston et al., 2014; Tessalina et al., 2016).

Moreover, understanding of common Pb is a necessity for corrections in U-Pb geochronology (e.g., Ludwig, 2012; Harrison et al., 2015). The non-radiogenic Pb component in any dated U-bearing mineral must be successfully accounted for in the total Pb measurements to accurately calculate radiogenic production, and thus a geologically meaningful age (Ludwig, 2012). Hence, accurate crustal Pb isotope evolution models are important as they underpin many common Pb correction approaches used in U-Pb geochronology (e.g., Storey et al., 2006; Andersen et al., 2019).

In an effort to constrain the Pb isotope evolution of the Yilgarn Craton in Western Australia, we measured the $^{206}Pb/^{204}Pb$, $^{207}Pb/^{204}Pb$, and $^{208}Pb/^{204}Pb$ isotope ratios of K-feldspar from a transect of dated granite samples through this craton. We analyzed 16 samples, ten of which have igneous crystallization ages determined via U-Pb Sensitive High Resolution Ion Microprobe (SHRIMP) zircon geochronology (Fletcher & McNaughton, 2001; Dunphy et al., 2003; this study, appendices A and B). This transect stretches from the Youanmi Terrane in the west to the Burtville Terrane of the Eastern Goldfields Superterrane (EGST) in the east, and transits across the crustal-scale Ida Fault (Fig. 1, Table 1). The Yilgarn Craton is characterized by one of the largest exposures of preserved Archean lithosphere on Earth and has a rich endowment of economic minerals (e.g., Groves et al., 1989; Blewett et al., 2010). The craton has been extensively investigated using a range of isotope systems. Isotopic data together with a series of deep crustal seismic lines (e.g., Youanmi, EGF1 and 01AGS-NY1; see Goleby et al., 2006, and Wyche et al., 2013, for a compilation) define crustal-scale boundaries (e.g., Cassidy et al., 2006; Wyche et al., 2012; Fig. 1) and make the Yilgarn Craton an excellent case study region to test the suitability of different Pb isotope evolution models. Furthermore, the Yilgarn Craton provides a window into the evolution of Archean crust, archiving a period of time when tectonics were likely driven by a combination of horizontally and vertically directed forces (e.g., Bédard, 2006; Van Kranendonk et al., 2007; Bédard et al., 2013, and references therein).

The Archean granites of the Yilgarn Craton represent an advantageous sampling medium for several reasons. Firstly, granites are a very direct link to crust-forming processes in general, and they occur in large volumes (Zartman & Wasserburg, 1969; Champion, 2013; Johnson et al., 2017; Halla, 2018). Secondly, K-feldspar is a prevalent framework mineral in all but the most sodic granites and an important Pb-bearing phase in granitic rocks. Thirdly, K-feldspar can be used as a powerful common Pb isotope tracer, as it incorporates Pb (Pb^{2+} can replace potassium cations; Heier, 1962) but essentially no U and Th during growth (e.g., Tyrrell et al., 2006, 2012). Thus, the Pb isotopic composition of K-feldspar is expected to not change

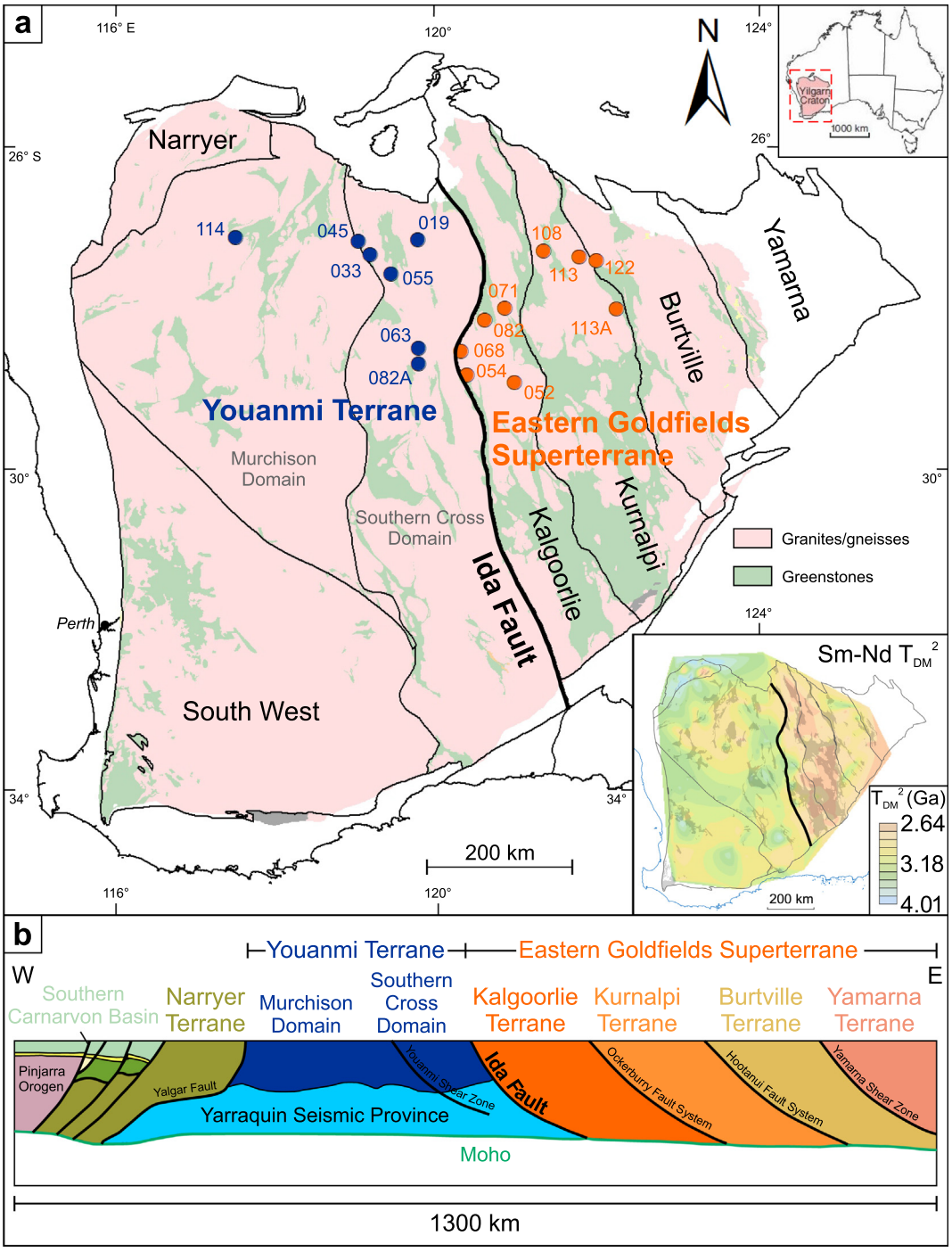

Fig. 1. a) Schematic map of the Yilgarn Craton with terranes, domains and simplified geology (granites vs. greenstones). Sample locations west of the Ida Fault are indicated in blue, while sample locations east of the Ida Fault are indicated in orange. The last three numbers of each sample ID are shown on the map (Tables 1, 2, and 3). The bottom right inset is a Nd two-stage model age map after Cassidy & Champion (2004), Champion & Cassidy (2007), Champion (2013), Mole et al. (2013), and Wyche et al. (2019). Two-stage Nd model ages were calculated as reported in these references. b) Generalized cross-section through the Yilgarn Craton; modified after Korsch et al. (2013). The east-dipping Ida Fault separates older, Mesoarchean lithosphere in the western Yilgarn Craton from younger, Neoarchean lithosphere in the Eastern Goldfields Superterrane. (For interpretation of the references to colour in this figure legend, the reader is referred to the web version of this article.)

Table 1
Coordinates and petrography of the granite samples.

Geoscience Australia (GA) Sample ID	Terrane	GDA94 Latitude (decimal degrees)	GDA94 Longitude (decimal degrees)	Approx. distance from the Ida Fault [km]	Lithology	Geoscience Australia (GA) Classification	Condition of the K-feldspar	Analysis session (date)
West of the Ida Fault								
99967114	Youanmi	−27.132578	117.450157	274 west	Biotite, fine-grained, porphyritic granodiorite	Low-Ca granite	2	20/03/2020
98969045	Youanmi	−27.170607	118.986389	122 west	Biotite, medium-grained, foliated monzogranite	Hi-Ca granite	2	15/06/2020
98969033	Youanmi	−27.338999	119.128387	110 west	Banded, foliated, porphyritic granite	Hi-Ca granite	2	20/03/2020
98969055	Youanmi	−27.585615	119.395386	92 west	Biotite, medium-grained, foliated monzogranite	Hi-Ca granite	2	20/03/2020
97969063	Youanmi	−28.510733	119.738556	52 west	Biotite, porphyritic, medium-grained monzogranite	Low-Ca granite	1	20/03/2020
97969082A	Youanmi	−28.710308	119.732529	50 west	Biotite, phyric, feldspar monzogranite	Felsic intrusives	1	15/06/2020
98969019	Youanmi	−27.155703	119.723389	49 west	Biotite, medium-grained, porphyritic monzogranite	Low-Ca granite	2	20/03/2020
East of the Ida Fault								
92969068	Kalgoorlie	−28.544485	120.270181	0.2 east	Biotite monzogranite		1	20/03/2020
92969054	Kalgoorlie	−28.848558	120.34415	6 east	Biotite monzogranite		1	20/03/2020
92969082	Kalgoorlie	−28.156521	120.567360	15 east	Biotite, porphyritic, medium-grained granite	Low-Ca granite	1	20/03/2020
92969071	Kalgoorlie	−28.00689	120.81043	32 east	Biotite monzogranite		1	15/06/2020
92969052	Kalgoorlie	−28.938266	120.936933	53 east	Biotite monzogranite		1	20/03/2020
2001969108	Kurnalpi	−27.296012	121.300693	92 east	Porphyritic biotite granite		1	20/03/2020
2001969113	Kurnalpi	−27.366487	121.743159	129 east	Sphene-biotite granite		1	20/03/2020
2001969122	Burtville	−27.414682	121.952995	147 east	Biotite, medium-grained, gneissic granodiorite	Hi-Ca granite	3	19/03/2020
92969113A	Kurnalpi	−28.016470	122.207344	167 east	Biotite, porphyritic, gneissic granodiorite	Hi-Ca granite	3	19/03/2020

Feldspar conditions: 1: The vast majority of the K-feldspar is pristine and shows only slight signs of alteration; 2: In places pristine looking K-feldspar, but also moderate signs of alteration in the grains; 3: K-feldspar appears strongly altered and/or contains strongly developed patterns that indicate recrystallization.

significantly with time. Hence, the K-feldspar Pb isotope signature, if unaltered, can provide a good approximation of the U/Pb and Th/Pb ratio of the source at crystallization. Existing common Pb studies from the Yilgarn Craton typically focused on the genesis of gold deposits throughout the EGST (e.g., Browning et al., 1987; Perring & McNaughton, 1992; McNaughton & Groves, 1996, and references therein). Specifically, many of these studies used Pb isotopes in Pb-rich ore minerals to assess the crustal or mantle contributions to mineralizing fluids. McNaughton & Groves (1996) reviewed and compiled preexisting Pb isotope data for the Yilgarn Craton and developed a compositional common Pb model for this region.

In this paper, we link new K-feldspar Pb isotope results to grain-scale trace element analyses of U and Th, whole rock geochemistry, and Nd isotopes (Champion et al., 2007; Champion, 2013) for the same U-Pb dated granite samples. Linking these data sets allows us to determine whether the source information yielded by granite K-feldspar Pb isotopes is consistent with other isotopic systems. We build on contributions that investigated the Pb isotopic patterns in ore systems in the Yilgarn Craton (Browning et al., 1987; Huston et al., 2005; Huston et al., 2014; Champion & Huston, 2016). These previous authors have documented a spatial correlation between Pb isotope patterns established from ore Pb with the Nd isotopic data determined from granites. Ore deposits are mostly related to hydrothermal fluid flow in the mid to upper crust, while Nd and Hf model ages are considered to reflect the average age of source component extraction from the mantle. Our study aims to enhance understanding of the crustal structure and Pb isotope evolution of the Yilgarn Craton and aid in assessing the potential of Pb-in-granite K-feldspar to provide geologically meaningful magma source constraints.

2. Pb ISOTOPE FRAMEWORK

This section gives a brief overview of the principles of Pb isotopes and Pb growth. A more detailed framework for Pb isotopes as context for the new results is provided in appendix C. Pb evolution models make predictions about the evolving Pb isotope composition of different geochemical reservoirs (i.e., mantle, crust, etc.) through time based upon a primordial Pb composition and a start date or system closure time t_1 (e.g., Oversby, 1974). The Pb isotope composition at any given time (t_2) in each decay system is described by the following general equations, which can be used to depict Pb growth curves:

$$\left(\frac{^{206}Pb}{^{204}Pb}\right)_{t_2} = \left(\frac{^{206}Pb}{^{204}Pb}\right)_{t_1} + \mu \times \left(e^{\lambda_x t_1} - e^{\lambda_x t_2}\right) \quad (1)$$

$$\left(\frac{^{207}Pb}{^{204}Pb}\right)_{t_2} = \left(\frac{^{207}Pb}{^{204}Pb}\right)_{t_1} + \left(\frac{\mu}{137.818}\right) \times \left(e^{\lambda_y t_1} - e^{\lambda_y t_2}\right) \quad (2)$$

$$\left(\frac{^{208}Pb}{^{204}Pb}\right)_{t_2} = \left(\frac{^{208}Pb}{^{204}Pb}\right)_{t_1} + \omega \times \left(e^{\lambda_z t_1} - e^{\lambda_z t_2}\right) \quad (3)$$

The parameter μ is defined as the $^{238}U/^{204}Pb$ ratio in the reservoir being modelled and ω is the $^{232}Th/^{204}Pb$ ratio. 137.818 ± 0.045 refers to the recent $^{238}U/^{235}U$ ratio after Hiess et al. (2012) based on the average of zircon analyses and is assumed to be a suitable proxy for the continental crust. This literature value is established in the geochronological community, since it is considered representative of the average uranium isotopic composition of Earth's bulk continental crust (Livermore et al., 2018). We use this value (137.818) for all calculations after different Pb evolution models in this paper. The λ parameters are the decay constants for the uranium isotopes ^{238}U ($\lambda_x = 1.55125 \times 10^{-10} \pm 0.00166 \times 10^{-10}$ yr^{-1}) and ^{235}U ($\lambda_y = 9.8485 \times 10^{-10} \pm 0.0135 \times 10^{-10}$ yr^{-1}) after Jaffey et al. (1971), and for the thorium isotope ^{232}Th ($\lambda_z = 4.9475 \times 10^{-11} \pm 0.0495 \times 10^{-11}$ yr^{-1}) suggested by Steiger & Jaeger (1977).

In magmatic systems, Pb-rich minerals that contain little to no U and Th (such as K-feldspar) will not in-grow significant radiogenic Pb and should preserve the initial Pb isotope composition of the magmas from which they crystallized. Different geological reservoirs characterized by different U-Th-Pb fractionation histories will have different U/Pb, Th/Pb, and Th/U ratios that are approximated by the derivative parameters μ, ω, and κ (defined as $^{232}Th/^{238}U$). Differences in these parameters will manifest as differences in observed spatial and/or temporal trends in Pb isotope composition with time.

The definition of a Pb evolution model requires the quantification of all parameters – typically by best-fitting growth curves through Pb ore sample sets of different known ages (e.g., Oversby, 1974; Stacey & Kramers, 1975). An abrupt change in μ or ω at a specific time can be modelled by introducing a separate second stage to a Pb evolution model. Several one-stage and two-stage models that describe global Pb evolution have been developed (Holmes, 1946; Houtermans, 1946; Stacey et al., 1969; Cumming & Richards, 1975; Stacey & Kramers, 1975; Doe & Zartman, 1979; Zartman & Doe, 1981; Zartman & Haines, 1988; Kramers & Tolstikhin, 1997), among which Stacey & Kramers' (1975) has been the most widely and frequently applied for common Pb correction in U-Pb geochronology (e.g., Storey et al., 2006; Andersen et al., 2019). This two-stage Pb evolution curve has been considered a globally appropriate model throughout Earth's history.

The term Bulk Silicate Earth describes the silicate part of the Earth – i.e., the crust and the mantle – as a theoretical closed reservoir after core formation and accretion (e.g., Kumari et al., 2016). In order to address limitations and shortcomings in the preexisting Pb evolution models, Maltese & Mezger (2020) reviewed published element abundance and Pb isotope data and chose the collision of proto-Earth with Theia at approximately 4.498 Ga as the start date for an evolution model of the Bulk Silicate Earth. This model displays internally consistent Pb evolution related to known geological processes that are thought to have affected Earth's U-Pb system. The model is based on the idea that the moon-forming Theia collision significantly modified the initial Pb (and subordinate U) content on Earth, from which Pb isotope ratios evolved to present-day compositions in a continuous single-stage development. The primordial Pb compositions and μ (= 8.63) and ω (= 34.8) values are distinct compared to Stacey & Kramers' (1975) model.

In plots of $^{207}Pb/^{204}Pb$ vs. $^{206}Pb/^{204}Pb$, the Pb isotope evolution of a reservoir with given U/Pb is depicted by a growth curve that describes how Pb isotope compositions change with time. The range of possible initial Pb isotope compositions for rocks of a given age defines straight lines, termed paleogeochrons, that intersect the growth curve at the crystallization age. The veracity of different Pb isotope evolution models depends on their ability to reproduce the initial isotopic composition of natural rock samples. Therefore, these models may be tested by analyzing the initial Pb isotope compositions ($^{206}Pb/^{204}Pb$, $^{207}Pb/^{204}Pb$, and $^{208}Pb/^{204}Pb$ ratios) of samples of known age and comparing these results to predictions from different models. Such an analysis may also be used to calculate average μ and ω values and define Pb evolution curves for specific geological regions.

3. GEOLOGICAL BACKGROUND OF THE YILGARN CRATON

The Meso- to Neoarchean Yilgarn Craton comprises a classic granite-greenstone stratigraphy (Wyche & Wyche, 2017). Approximately one-third of the craton is represented by mostly north–south-trending supracrustal greenstone successions, with granitic rocks and gneisses constituting the remaining two-thirds (Mole et al., 2019). The craton covers an area of approximately 650 000 km^2 (total exposure area) and has been subdivided into seven north–south elongate terranes (Cassidy et al., 2006; Pawley et al., 2012; Figure 1a). Its magmatic components have been extensively dated using zircon U-Pb geochronology and its crustal structure elucidated via Sm-Nd and Lu-Hf isotopic studies (Champion & Sheraton, 1997; Cassidy & Champion, 2004; Champion & Cassidy, 2007; Czarnota et al., 2010; Champion, 2013; Mole et al., 2012, 2013, 2014, 2019; Fig. 1a). Terranes define crust sharing similar stratigraphy, or corresponding petrographic, geochemical, and age trends, and are subdivided into fault-bounded, geologically contiguous domains (Swager et al., 1992). Nd isotopic maps have significantly contributed to the definition of different crustal domains in the Yilgarn Craton (Fig. 1a) and also aided in defining areas of metal enrichment (Champion, 2013; Champion & Huston, 2016).

Mole et al. (2019) presented a zircon Hf-isotope-based evolution history for the Yilgarn Craton involving three major mantle input events (at ca. 3.0–2.9, 2.8 and 2.7 Ga). Eventually, the Yilgarn Craton stabilized with the isotopic signature reflecting an interplay of juvenile mantle input and older continental lithosphere (>3.0 Ga) (Mole et al., 2019). Syn- to post-tectonic craton-wide extension led to the intrusion of all terranes by granitic melts between ~2700 and 2600 Ma (Czarnota et al., 2010; Mole et al., 2012). The Youanmi Terrane in the western Yilgarn Craton has traditionally been referred to as the ancient protocontinent (nucleus) of the craton (Cassidy & Champion, 2004). Models such as those of Groves & Batt (1984) suggested rift-like settings for the Yilgarn Craton. The interpretation that the four terranes of the Eastern Goldfields Superterrane (EGST) have been successively accreted and amalgamated to the Youanmi Terrane protocontinent was prominent during the 1990s (e.g., Myers, 1995). Yet there is increasing evidence that the Youanmi Terrane extends beneath the EGST, and consequently represents the basement to the younger part of the craton (Pawley et al., 2012; Wyche et al., 2012; Van Kranendonk et al., 2013; Morris & Kirkland, 2014; Mole et al., 2014). Pawley et al. (2012) suggested a common history of the Youanmi Terrane and the Burtville Terrane back to c. 2970 Ma, based on zircon Hf isotope data, highlighting the role of rifting and reassembly.

The South West, Narryer, and Youanmi terranes form the western part of the Yilgarn Craton (Fig. 1). Granites and granitic gneisses are predominant in the South West and in the Narryer Terrane (Wyche & Wyche, 2017). With subordinate components dated as old as ~3730 Ma (e.g., Nutman et al., 1991), the Narryer Terrane encompasses the oldest known rocks of the Yilgarn Craton.

Within the Yilgarn Craton, the Ida Fault is a major, east-dipping structure extending to the base of the crust (e.g., Goleby et al., 2006). The fault dips at approximately 30-45° and marks a distinct lithospheric boundary between the western Yilgarn Craton and the EGST, separating younger, Neoarchean lithosphere in the east from older, Mesoarchean (> 3.0 Ga) lithosphere in the west (e.g., Swager et al., 1997; Blewett et al., 2010; Fig. 1b). The Ida Fault is clearly imaged as a Nd (whole rock) and Hf (zircon) isotopic boundary between more evolved crust in the west versus more juvenile crust in the east. The fault is also resolved on seismic images (Goleby et al., 2006; Blewett et al., 2010; Wyche et al., 2013).

The EGST in the east of the craton is an Archean granite-greenstone terrane, that formed between ~2940 and 2600 Ma (Squire et al., 2010). The majority of the rocks in the EGST, including the granites and greenstones, are younger than 2690 Ma. The EGST has a rich endowment of gold (e.g., Groves et al., 1989; Blewett et al., 2010). It also hosts significant nickel sulfide and lithium-tantalum deposits, as well as a few volcanic-hosted massive sulfide (VHMS) base metal deposits (Wyche et al., 2012; Huston et al., 2014). This Superterrane comprises four terranes from west to east: Kalgoorlie, Kurnalpi, Burtville, and Yamarna (Pawley et al., 2012) that are separated from one another by major east-dipping faults and shear zones (Fig. 1b). Some of these boundaries have been intruded by granitic melts.

4. METHODS

Granitic rocks samples investigated in this work have been dated by U-Pb zircon geochronology using the Geoscience Australia (GA) Sensitive High Resolution Ion Microprobe (SHRIMP II). A detailed description of the U-Pb zircon technique and related analytical procedures is provided in appendix A (Fletcher & McNaughton, 2001; Dunphy et al., 2003).

A Tescan Integrated Mineral Analyzer (TIMA), based around a scanning electron microscope with an array of EDX detectors, was used to characterize mineral phases in the 16 samples in polished epoxy rounds prior to isotopic analysis. The $^{206}Pb/^{204}Pb$, $^{207}Pb/^{204}Pb$, and $^{208}Pb/^{204}Pb$ ratios of K-feldspar in the sample set were determined

during three analytical sessions, using Laser Ablation Multi-Collector Inductively Coupled Plasma Mass Spectrometry (LA-MC-ICPMS) in the John de Laeter Centre (JdLC) at Curtin University in Perth. Between 32 and 48 spots per sample were conducted with a spot size of 50 μm. A detailed description of the analytical setup and the reference materials of this research – the K-feldspar reference material Kf-Shap (Tyrrell et al., 2006), an in-house Albany feldspar standard, and NIST 612 glass (Hollocher & Ruiz, 1995; Pearce et al., 1997) – is presented in appendix D. Measured and recommended values for the secondary Albany reference material are provided in appendix E.

Owing to limitations imposed by the configuration of detectors on the multi-collector instrument it was not possible to measure U and Th ion-beams concurrently with the various Pb isotopes. Therefore, concentrations of U and Th were measured on spots adjacent to each Pb isotope analysis, in the same textural domain, in a separate analytical session using an Agilent 8900 triple quadrupole mass spectrometer employing a spot size of 50 μm. The glass standards NIST 610 and NIST 612 (Hollocher & Ruiz, 1995; Pearce et al., 1997) were used as reference materials for concentration determination. NIST 612 was the primary reference material, whereas NIST 610 was used to verify results. Appendix F contains data tables with the analyzed trace element concentrations of U and Th.

Pb isotopic data were reduced in iolite 4.3.8 (Paton et al., 2011) through a data reduction scheme that performs an Hg interference correction (Delavault et al., 2018) and yields corrected isotope ratios, Pb concentrations, and the $^{204}Hg/^{204}Total$ ratio as a measure of the magnitude of the Hg interference correction. Hg correction was based on measured ^{202}Hg and an assumed relative $^{204}Hg/^{202}Hg$ abundance of 0.22988 which was used to estimate ^{204}Hg that was removed from ^{204}Pb. We did not observe correlations between Pb isotope ratios and Hg content in data from primary K-feldspar (see appendix G for a $^{206}Pb/^{204}Pb$ vs. $^{204}Hg/^{204}Total$ ratio plot of all primary data points). Absolute 2σ errors include internal and external sources of error propagated in quadrature. We corrected for Pb isotope fractionation using sample-standard bracketing.

In order to assess the condition of K-feldspar in each sample (Table 1), a Hitachi TM3030 SEM (scanning electron microscope) was used for back-scattered electron imaging of targeted feldspar. Significant heterogeneities in some common Pb signatures reflect Pb loss or Pb mixing induced by alteration. Such altered feldspar can be successfully filtered using these following criteria: Variability in the measured isotope ratios that manifests as elevated errors, such as an absolute propagated error ≥ 0.2 for $^{206}Pb/^{204}Pb$ and $^{207}Pb/^{204}Pb$ and absolute propagated error ≥ 0.4 for $^{208}Pb/^{204}Pb$ analyses. Significant variabilities in the Pb ratios were found to be associated with high Hg content ($^{204}Hg/^{204}Total \geq 5\%$) and low Pb content ($\leq 10$ ppm). Primary igneous K-feldspar data remaining after this filtering step are assigned to groups A and B, excluded data points showing secondary signatures are termed group C. In the case of two metamorphic samples 2001969122 and 92969113A elevated Hg content was observed and specifically discussed below.

Data are also filtered to remove analyses with elevated U and Th content (^{238}U and/or $^{232}Th \geq 0.5$ ppm) (Fig. 2 and Table 2). Relatively small amounts of U can have a significant effect on the Pb isotopic ratios in conjunction with the average Pb content of K-feldspar in our samples (Fig. 2). Data points removed in this second filtering step were assigned to group B. This filtering for U and Th content in K-feldspar ensures a population of Pb data unaffected by radiogenic ingrowth (Fig. 2). Pb model ages in this study are used to characterize source compositions (Milot et al., 2021) and provide additional information to complement interpretations of absolute crystallization age constraints. Pb model ages presented in Table 2 for each individual sample were calculated using equations outlined by Albarède et al. (2012). We used the median $^{206}Pb/^{204}Pb$, $^{207}Pb/^{204}Pb$, and $^{208}Pb/^{204}Pb$ ratios of group A data for each individual sample as input values to these equations. Pb model ages were calculated using two different Pb evolution models: Maltese & Mezger's (2020) single-stage and Stacey & Kramers' (1975) two-stage Pb model (Table 2).

Data tables of common Pb analyses in reference materials and samples are provided in appendix H and common Pb plots of each individual sample with paleogeochrons after different Pb evolution models in appendix I.

μ, ω, and κ values after Maltese & Mezger (2020) were calculated for each individual data point (excluding secondary group C data) using the $^{206}Pb/^{204}Pb$, $^{207}Pb/^{204}Pb$, and $^{208}Pb/^{204}Pb$ ratios and the known granite age of the samples. The median of all mean μ values (μ_{206} (Eq. (D.1)) and μ_{207} (Eq. (D.2)); appendix D), and median ω (Eq. (D.3); appendix D) and κ (Eq. (D.4); appendix D) values of each individual sample are listed in Table 3. We determined the average of all medians of these derivative parameters for samples from west and east of the Ida Fault and accompanied uncertainties using standard deviations.

5. SAMPLES

In this contribution we examine 16 Archean granite samples from the Youanmi, Kalgoorlie, Kurnalpi, and Burtville terranes in the Yilgarn Craton, ten of which have igneous crystallization ages constrained via U-Pb SHRIMP zircon geochronology and the remaining six have geologically well-established ages. The samples were taken along a ~460 km west-east transect crossing the Ida Fault. Seven of the samples were taken west of the Ida Fault in the Youanmi Terrane and the remaining nine samples were taken east of the fault in the EGST (Fig. 1a and Table 1).

15 of the analyzed samples have reported crystallization ages from 2712 Ma to 2630 Ma (Table 2). The U-Pb age of sample 2001969122 is significantly older (2939 ± 6 Ma). Six of the U-Pb zircon datasets are published (Fletcher & McNaughton, 2001; Dunphy et al., 2003); the remaining four comprise two Fletcher & McNaughton (2001) datasets, which we reinterpret to estimate an igneous crystallization age, and a further two U-Pb datasets (sample IDs 92969082 and 92969113A) are presented in this work. Details of the newly presented zircon U-Pb data (together with tabular isotopic data and its interpretation for all 10 samples) are included in appendices A and B. Those

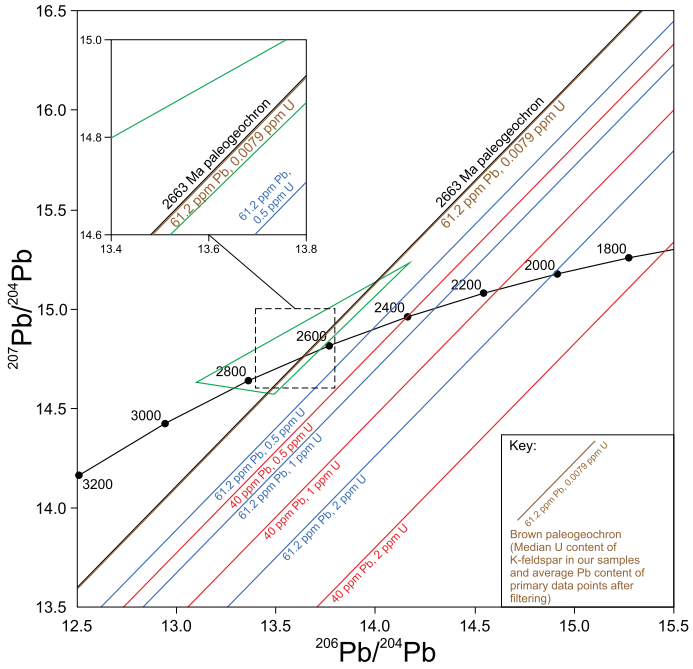

Fig. 2. $^{207}Pb/^{204}Pb$ vs. $^{206}Pb/^{204}Pb$ plot that illustrates the minor effect of U in K-feldspar in our samples and the effect of different U and Pb contents in K-feldspar on Pb isotopic results. The black Pb growth curve is Maltese & Mezger's (2020) Pb evolution model for the Bulk Silicate Earth. The green triangle is the compositional Pb source model for the Eastern Goldfields Superterrane after McNaughton & Groves (1996). The black 2663 Ma paleogeochron represents an example data point array for the average U-Pb granite crystallization age of our samples (excluding samples 99967114, 2001969122, and 92969113A that are discussed as separate case studies). The brown paleogeochron that mostly overlaps with the 2663 Ma paleogeochron shows that the effect of the median U content in our samples – combined with the average Pb content of data points after filtering (again excluding samples 99967114, 2001969122, and 92969113A) – is negligible. Different paleogeochrons exemplify the impact of 0.5 ppm, 1 ppm, and 2 ppm U content for a typical Pb concentration in K-feldspar (40 ppm; red paleogeochrons) and for the average Pb content of data points after filtering in our samples (61.2 ppm; blue paleogeochrons). We calculated μ ($^{238}U/^{204}Pb$) in order to shift the black paleogeochrons towards more radiogenic compositions using the natural abundance of ^{238}U (99.2745%) and ^{204}Pb (1.4%) and the atomic weight of U and Pb. This figure illustrates that comparatively small amounts of U can significantly affect Pb isotopic data from K-feldspar; U in our sample set, however, does not influence data to a meaningful degree (also compare the arrays of common Pb data points for individual samples in appendix I). (For interpretation of the references to colour in this figure legend, the reader is referred to the web version of this article.)

samples which have not been directly dated using zircon U-Th-Pb dating, in this work or previously, have ages well-established via regional stratigraphic constraints (age reference E in Table 2; e.g., Champion & Sheraton, 1997; Champion & Cassidy, 2002).

The TIMA mineral phase maps allow petrographic classification of the 16 investigated samples as syenogranites, monzogranites, and granodiorites. Samples 2001969122 and 92969113A are gneissic granodiorites. Plagioclase is the most common mineral in the samples that also contain abundant K-feldspar, quartz, and in many cases moderate proportions of biotite in the form of biotite-rich enclaves or banding. The samples are predominantly fine- to medium-grained. Rock textures are porphyritic or granophyric. K-feldspar varies from unaltered and crystalline, to heavily altered and weathered, and in places also includes recrystallized domains (Table 1; K-feldspar SEM images provided in appendix J). Despite apparent alteration and weathering effects, inspection of the analyzed K-feldspar through back-scattered electron imaging did not reveal signs of kaolinitization, which could result in zones of elevated U content and production of radiogenic Pb, nor sericitation. Geochemically, the samples belong to two major groups: high-Ca (~TTGs) and low-Ca (potassic) granitic rocks (Champion & Sheraton, 1997; Cassidy & Champion, 2004).

6. RESULTS

A plot provided in appendix G demonstrates that there is no relationship between Hg content and Pb isotopic ratios in our sample set, except for sample 99967114 with elevated Hg content, which is discussed as a specific case study.

Fig. 2 illustrates the effect of different U and Pb contents in K-feldspar on the initial Pb ratios. We calculate the effect of 0.5 ppm, 1 ppm, and 2 ppm U on the 2663 Ma paleogeochron in $^{207}Pb/^{204}Pb$ vs. $^{206}Pb/^{204}Pb$ space. We use 2663 Ma for the paleogeochron, the average crystallization age of the 13 non-altered igneous samples. Calculations were conducted for two different Pb contents: 40 ppm Pb – a typical concentration in K-feldspar (e.g., Tyrrell et al., 2006, and Zhang et al., 2014, and references therein; red paleogeochrons in Fig. 2) - and 61.2 ppm Pb, the average Pb concentration of primary feldspar in this Yilgarn Craton sample set (Table 2; blue paleogeochrons in Fig. 2). The

Table 2
U-Pb zircon and estimated crystallization ages, and calculated Pb model ages of the granite samples.

Geoscience Australia (GA) Sample ID	Granite age [Ma] (Age reference)	± 95% conf. [Ma]	n	$n_{primary}$	Mean Pb content $n_{primary}$ [ppm]	Median $^{204}Hg/^{204}$Total Ratio	$n_{U\text{-}Th}$	Pb model age SK [Ma]	Pb model age MM [Ma]
West of the Ida Fault									
99967114	2630 (B)	50	42	14	56.10	0.024	14	2711	2538
98969045	2700 (A)	15	40	36	52.51	0.029	36	2860	2672
98969033	2671 (A)	3	32	31	54.00	0.027	30	2933	2681
98969055	2712 (A)	6	32	27	49.22	0.028	27	2953	2736
97969063	2684 (A)	8	40	36	54.01	0.029	28	2910	2702
97969082A	2682 (A)	5	40	38	40.85	0.031	33	2989	2734
98969019	2640 (B)	50	44	24	64.98	0.023	20	2857	2610
East of the Ida Fault									
92969068	2640 (E)		40	35	65.48	0.024	30	2940	2706
92969054	2640 (E)		48	45	101.61	0.015	36	2873	2673
92969082	2665 (D)	5	40	37	57.65	0.022	37	2900	2682
92969071	2650 (E)		40	37	88.70	0.016	37	2871	2671
92969052	2650 (E)		42	38	65.85	0.023	36	2888	2678
2001969108	2650 (E)		42	40	60.29	0.025	34	2815	2658
2001969113	2640 (E)		43	37	40.30	0.036	35	2743	2634
2001969122	2939 (C)	6	39	29	33.71	0.098	26	3015	2774
92969113A	2671 (D)	12	41	39	29.45	0.100	39	2963	2772

Granite age references: (A) = U-Pb SHRIMP zircon date in Fletcher & McNaughton (2001); (B) = Geoscience Australia estimate, based on U-Pb SHRIMP zircon data presented by Fletcher & McNaughton (2001); (C) = U-Pb SHRIMP zircon date in Dunphy et al. (2003); (D) = New U-Pb SHRIMP zircon data presented herein; (E) = Estimated; no U-Pb zircon data available.
n: number of spots.
$n_{primary}$: number of primary data points after filtering (group A and B data).
Median $^{204}Hg/^{204}$Total Ratio: Median of $^{204}Hg/^{204}$Total of all primary data points (group A and B data) calculated through an in-house data reduction scheme for iolite 4.
$n_{U\text{-}Th}$: number of data points used for the calculation of a Pb model age (group A data) after filtering for U and Th content $\geq$ 0.5 ppm in a secondary filtering step.
Pb model age SK: Pb model age after Stacey & Kramers' (1975) two-stage Pb evolution model; calculated after Albarède et al. (2012).
Pb model age MM: Pb model age after Maltese & Mezger (2020); calculated after Albarède et al. (2012).

median U content of analyzed K-feldspar is very low in every individual sample and its influence on Pb isotopic results is considered negligible (see Fig. 2 and Table 3) and a time-correction for ingrowth is not required. Only 45 of 569 data points investigated for element concentrations are excluded on the basis of elevated U and/or Th from Pb model age calculations.

Having demonstrated that Hg interference and U content in K-feldspar has negligible effects on Pb isotopic ratios in our sample set, we interpret the data point arrays to reflect geological processes. Hence, we assume that variability in Pb isotopic data documents heterogeneity in source U/Pb and Th/Pb.

The bulk of common Pb data acquired in this study falls on paleogeochrons after Maltese & Mezger (2020). The Pb isotopic compositions of samples taken in the Youanmi Terrane west of the Ida Fault form two distinct linear arrays in the $^{207}Pb/^{204}Pb$ vs. $^{206}Pb/^{204}Pb$ plot (Fig. 3a), the younger of which is approximated by a 2682 Ma reference paleogeochron (the average granite crystallization age of the samples) using the Maltese & Mezger (2020) Pb isotope evolution model. A 2730 Ma paleogeochron similarly corresponds to an older linear trend in the data, while a weaker and younger trend is approximated by a 2630 Ma reference paleogeochron (Fig. 3a). There is significantly more scatter in the data towards less radiogenic $^{206}Pb/^{204}Pb$ and $^{207}Pb/^{204}Pb$ compositions from samples west of the Ida Fault before filtering of group C data; however, after filtering variability is comparable between west and east of the Ida Fault (Fig. 3a). Data of the westernmost sample of this transect (99967114) scatter towards less radiogenic $^{206}Pb/^{204}Pb$ and $^{207}Pb/^{204}Pb$ compositions. The related Pb model age for sample 99967114 is interpreted to reflect alteration.

The $^{206}Pb/^{204}Pb$ and $^{207}Pb/^{204}Pb$ compositions of seven samples from east of the Ida Fault define a dominant trend that follows a reference 2683 Ma paleogeochron, which reflects the average granite crystallization age of the samples (Fig. 3a). A minority of the data plot towards higher $^{206}Pb/^{204}Pb$ ratios, and therefore towards younger model ages in a Pb evolution diagram. The majority of these data belong to sample 2001969113, a sample that has a significantly lower median μ and ω value. The data of sample 2001969122 together with those of sample 92969113A, the most easterly samples, form a separate distinct linear array that approximately corresponds to a 2770 Ma paleogeochron after Maltese & Mezger (2020).

Thorogenic common Pb data from the Youanmi Terrane displayed in a $^{208}Pb/^{204}Pb$ vs. $^{206}Pb/^{204}Pb$ plot (Fig. 3b) are similarly well approximated by Stacey & Kramers' (1975) and Maltese & Mezger's (2020) Pb evolution models. Collectively, the EGST data form one coherent linear trend. The two samples 2001969122 and 92969113A produce two separate arrays with relatively low ω values (Fig. 3b).

For 11 out of 16 samples using the Maltese & Mezger (2020) framework yields Pb model ages between 2610 Ma and 2736 Ma, consistent with the known crystallization ages of the granitic rocks (Table 2). For these 11 samples the differences between Pb model ages and granite crystallization ages vary from 6 Ma to 33 Ma (Table 2).

No data fall on a granite crystallization age paleogeochron after Stacey & Kramers (1975) (see Fig. 3 and common Pb plots in appendix I). Accordingly, calculating Pb model ages using the two-stage Stacey & Kramers' (1975) model framework yields ages that are older by 76 Ma to 307 Ma (on average > 200 Ma) compared to the known granite U-Pb crystallization ages (Figs. 3 and 4).

Three samples (99967114, 97969063, 92969068) yield Pb model ages (Maltese & Mezger, 2020) that are > 50 Ma older than their respective crystallization ages. The majority of data of samples 97969063 and 92969068 still plot on or close to the apparent crystallization age paleogeochrons. The calculated Pb model age (Maltese & Mezger, 2020) for sample 2001969122 is more than 150 Ma younger than its currently accepted U-Pb zircon crystallization age (2939 ± 6 Ma). Filtered data of this sample plot between the single-stage and the two-stage paleogeochron for the U-Pb zircon crystallization age after Stacey & Kramers (1975). The data of sample 92969113A fall on neither of the models' paleogeochrons, the Pb model age after Maltese & Mezger (2020) is 101 Ma older than the U-Pb granite crystallization age.

Our samples show a relatively close alignment with the global galena reference line in graphical linearization after Albarède & Juteau (1984), with the bulk of data points plotting below the reference line in $^{206}Pb/^{204}Pb$ space (Fig. 5a) and above the reference line for $^{207}Pb/^{204}Pb$ (Fig. 5b). Samples from the Youanmi Terrane show a tendency to higher $^{207}Pb/^{204}Pb$ ratios and to a lesser extent also to higher $^{206}Pb/^{204}Pb$ and $^{208}Pb/^{204}Pb$ ratios relative to EGST samples. There is a relatively clear distinction between Youanmi Terrane and EGST samples in inverted $^{208}Pb/^{204}Pb$ space with all but one Youanmi Terrane sample plotting above the galena reference line and the majority of EGST samples plotting below it (Fig. 5c). A negative correlation between $^{206}Pb/^{204}Pb$, $^{207}Pb/^{204}Pb$, and $^{208}Pb/^{204}Pb$ ratio and granite crystallization age is observed in the Youanmi Terrane samples. Linear least squares regressions of Youanmi Terrane Pb isotopic ratio and age are statistically significant ($^{206}Pb/^{204}Pb$, $p = 0.0010053$ [99.99% conf.], $r^2 = 0.90398$; $^{207}Pb/^{204}Pb$, [excluding 99967114 due to alteration], $p = 0.012353$ [99.9% conf.], $r^2 = 0.82414$; $^{208}Pb/^{204}Pb$, $p = 0.0022334$ [99.98% conf.], $r^2 = 0.86859$).

Calculated average μ is 8.93 ± 0.11 (all uncertainties are standard deviations) and ω is 38.24 ± 1.19 in samples from west of the Ida Fault and higher relative to the average μ of 8.72 ± 0.12 and ω of 36.55 ± 1.02 in samples from east of the Ida Fault. There is also a difference across the Ida Fault in κ with an average κ of 4.28 ± 0.09 in Youanmi Terrane samples and an average κ of 4.19 ± 0.07 in EGST samples.

7. DISCUSSION

7.1. A suitable Pb evolution framework for the Yilgarn Craton

In order to test the suitability of Stacey & Kramers' (1975) and Maltese & Mezger's (2020) Pb evolution models for the Yilgarn Craton we compare the arrays formed by

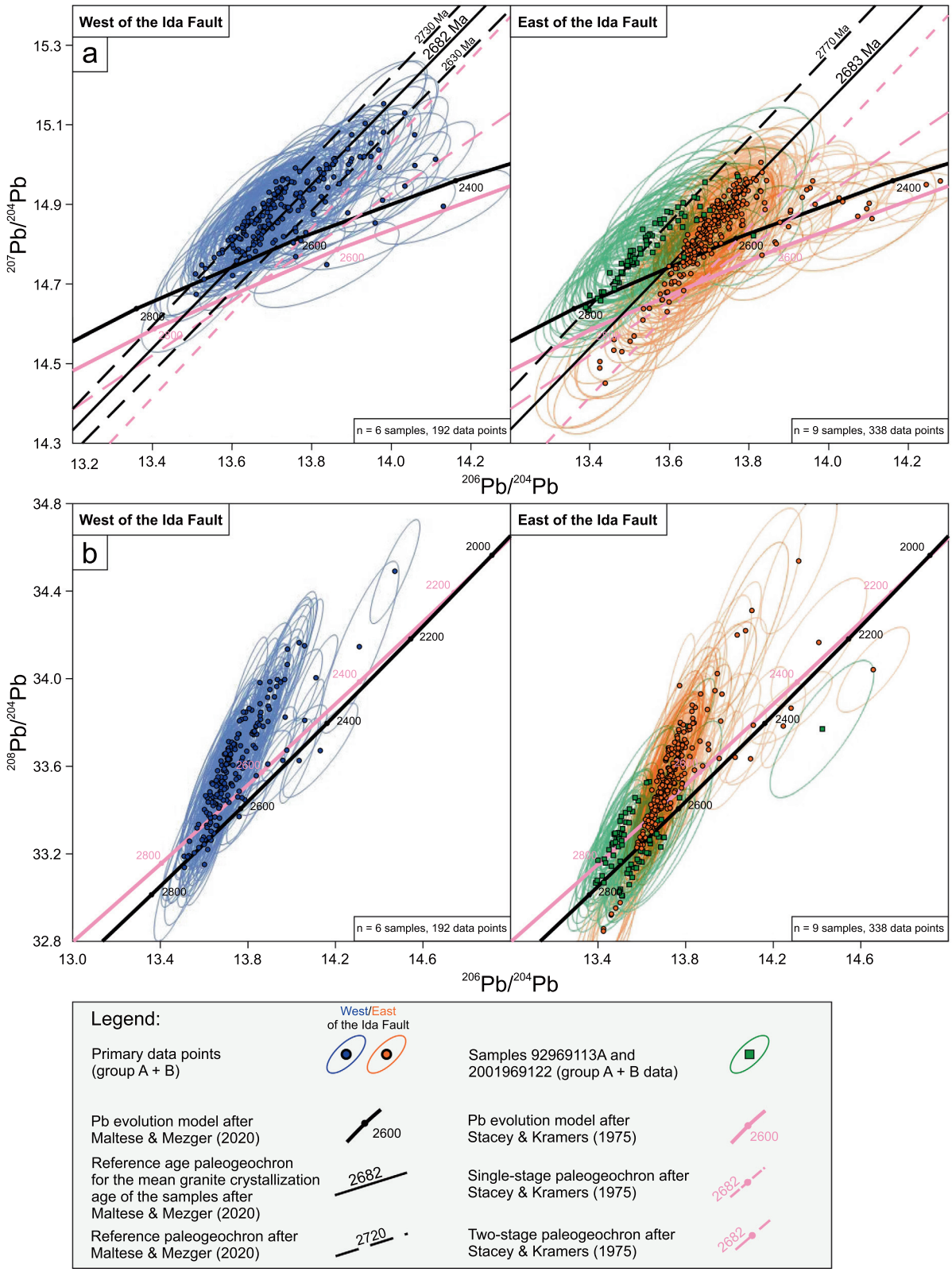

Fig. 3. a) $^{207}Pb/^{204}Pb$ vs. $^{206}Pb/^{204}Pb$ plots that show the primary data points (groups A + B) of all samples for west and east of the Ida Fault. The data points correspond well with Maltese & Mezger's (2020) Pb evolution model for the Bulk Silicate Earth on both sides of the Ida Fault in the Yilgarn Craton, but they are offset from Stacey & Kramers' (1975) model by ~80–150 Ma. The two samples 92969113A and 2001969122 from east of the Ida Fault form a distinct separate linear array approximately corresponding with a 2770 Ma paleogeochron after Maltese & Mezger (2020). As the data points of sample 99967114 scatter towards present-day Pb compositions and are discussed in the context of alteration, they are not displayed here. b) $^{208}Pb/^{204}Pb$ vs. $^{206}Pb/^{204}Pb$ plots with the primary data points (groups A + B) of all samples for west and east of the Ida Fault. The approximation of the main trends in thorogenic common Pb data by Stacey & Kramers' (1975) two-stage and Maltese & Mezger's (2020) single-stage Pb evolution model works similarly well. Error ellipses depict error correlations in all diagrams.

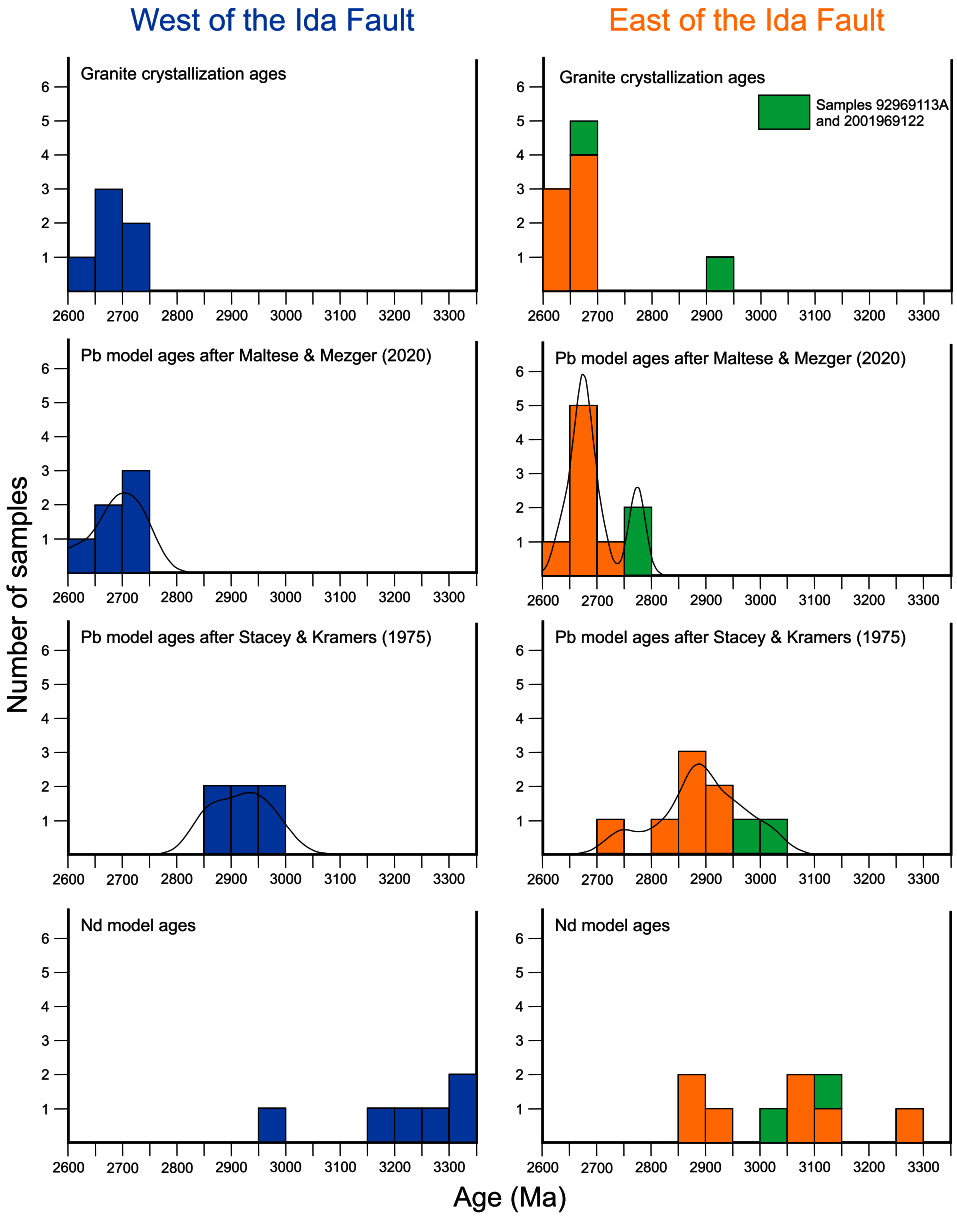

Fig. 4. Histograms comparing U-Pb crystallization ages with model ages yielded by the Pb and Sm-Nd isotopic systems. Pb model ages were calculated after equations published by Albarède et al. (2012) using two different Pb evolution models after Maltese & Mezger (2020) and Stacey & Kramers (1975). The Pb model age bins are plotted in conjunction with kernel density functions (black curves). We used Nd model ages of the samples from Champion (2013). Sample 99967114 was excluded from this figure, since the Pb model ages deduced from it are interpreted to have no geological meaning due to alteration effects.

analyses of our samples in $^{207}Pb/^{204}Pb$ vs. $^{206}Pb/^{204}Pb$ plots with constructed paleogeochrons for the known granite crystallization ages after the two models (see the individual common Pb plots provided in appendix I). Eleven out of 16 Yilgarn transect samples fall on the granite crystallization age paleogeochrons after Maltese & Mezger (2020). Common Pb results of none of our samples correspond with a paleogeochron after Stacey & Kramers (1975). Thus, our results indicate that the Pb evolution framework proposed by Maltese & Mezger (2020) makes a more accurate Pb growth prediction for the Yilgarn Craton than the Stacey & Kramers' (1975) model. A more quantitative test of this observation is demonstrated by the fact that model ages using the Maltese & Mezger (2020) framework yield results in agreement with granite crystallization ages determined through U-Pb zircon geochronology and stratigraphic constraints (Figs. 3a and 4). In contrast, Pb model ages calculated using the Stacey & Kramers' (1975) framework are significantly older (on average > 200 Ma) than U-Pb granite crystallization ages (Figs. 3 and 4). These results therefore demonstrate that the Maltese & Mezger (2020) model provides a far better approximation of the Pb isotope evolution of the Yilgarn Craton.

The apparent accuracy of the Maltese & Mezger (2020) model may support some underlying assumptions of that model; specifically, that a moon-forming collision of proto-Earth with Theia modified Earth's initial Pb content.

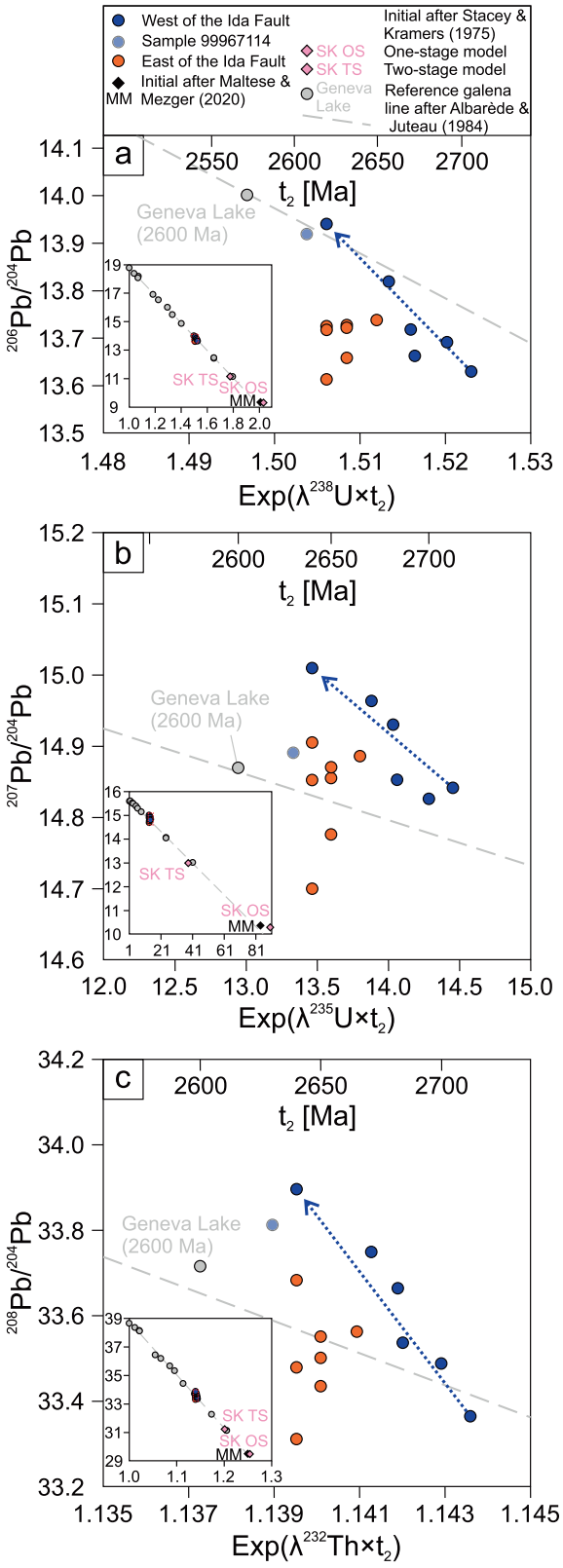

To date, Stacey & Kramers' (1975) two-stage Pb evolution model has been the standard and widely utilized for common Pb correction in U-Pb geochronology (e.g., Storey et al., 2006; Andersen et al., 2019). Our finding may be important in this regard, since it demonstrates that Maltese & Mezger's (2020) Pb evolution model can provide higher precision common Pb correction than Stacey & Kramers' (1975) model at least for the Yilgarn Craton.

In $^{208}Pb/^{204}Pb$ vs. $^{206}Pb/^{204}Pb$ space, Stacey & Kramers' (1975) and Maltese & Mezger's (2020) Pb evolution frameworks appear to make similarly good approximations of thorogenic Pb evolution in the Yilgarn Craton (Fig. 3b).

7.2. Pb growth in the Yilgarn Craton

We use the primordial Pb composition and timing (start date) of Maltese & Mezger's (2020) model and specific μ and ω values calculated based upon our results to describe

Fig. 5. Graphical linearization after Albarède & Juteau (1984) for $^{206}Pb/^{204}Pb$ (a), $^{207}Pb/^{204}Pb$ (b), and $^{208}Pb/^{204}Pb$ (c). The median $^{206}Pb/^{204}Pb$ ratio (of group A and B data) of each sample is plotted vs. $Exp(\lambda^{238}U\times t_2)$, the median $^{207}Pb/^{204}Pb$ ratio vs. $Exp(\lambda^{235}U\times t_2)$, and the median $^{208}Pb/^{204}Pb$ ratio vs. $Exp(\lambda^{232}Th\times t_2)$ – with t_2 as the known granite age of the samples. Granite ages (t_2) in Ma equivalent to the x-axis values are shown on the upper x-axis. Since Maltese & Mezger's (2020) Pb evolution model appears to provide a reasonable framework for the Yilgarn Craton, the start Pb composition of the model at 4.498 Ga is displayed in black in the insets to the bottom left of the three diagrams (red boxes illustrate the enlarged section) along with 14 reference galenas that Albarède & Juteau (1984) used to calculate and plot the best-fit linearization. The start compositions of Stacey & Kramers' (1975) one-stage (pink; at 4.57 Ga) and two-stage (pink; at 3.7 Ga) models are slightly offset from the linearizations. Our data set shows a good agreement with the global galena reference line after Albarède & Juteau (1984) in general (see insets). Overall, samples from the Youanmi Terrane (blue data points) have a tendency to higher $^{206}Pb/^{204}Pb$, $^{207}Pb/^{204}Pb$, and $^{208}Pb/^{204}Pb$ ratios relative to EGST samples (orange data points). All but one sample plot below the reference best-fit linearization in inverted $^{206}Pb/^{204}Pb$ space, while all but two EGST samples plot above this line in inverted $^{207}Pb/^{204}Pb$ space, indicating a certain deficit in radiogenic ^{206}Pb and a certain enrichment in radiogenic ^{207}Pb with respect to the global galena linearization. The majority of EGST samples shows a deficit in ^{208}Pb relative to the reference galenas, whereas Youanmi Terrane samples mostly plot above the $^{208}Pb/^{204}Pb$ linearization. A negative correlation between granite crystallization age and Pb ratios of Youanmi Terrane samples is seen in all three plots (indicated by dotted blue arrows). The sampled granite age range is narrow, especially in the EGST where granite sample ages range from 2665 Ma to 2640 Ma. Investigated Youanmi Terrane granites have crystallization ages between 2712 Ma and 2640 Ma. Sample 99967114 from the Youanmi Terrane is discussed in the context of possible alteration in this paper and depicted as half-transparent data point. The two samples 92969113A and 2001969122 are excluded from this figure because the K-feldspar Pb signatures in the samples are interpreted to have been affected by metamorphism, and the currently accepted granite crystallization age – a parameter influencing the x-axis values – is reinterpreted in this study.

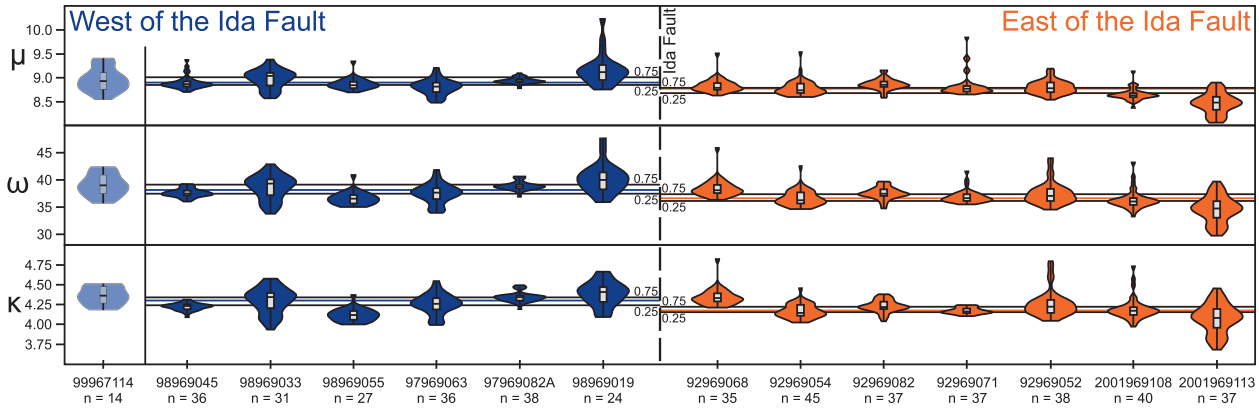

Fig. 6. Violin plot displaying the mean μ, ω, and κ of each individual sample (calculated after equations Eq. (D.1) to Eq. (D.4)) vs. the sample locality in relation to the Ida Fault. Secondary group C data were excluded from the calculation. n is the number of group A and B data in each sample. The median of all medians (blue and orange lines) and the 75% and 25% percentiles (black lines) of all samples are shown for both sides of the Ida Fault. Sample 99967114 (half-transparent violins) has not been included in the calculation of average and median values and percentiles, as its strongly scattered Pb data points are interpreted to reflect alteration. The two samples 92969113A and 2001969122 are excluded from this figure because the K-feldspar Pb signature in the samples, and thus also the μ, ω, and κ values, are interpreted to have been affected by metamorphism. (For interpretation of the references to colour in this figure legend, the reader is referred to the web version of this article.)

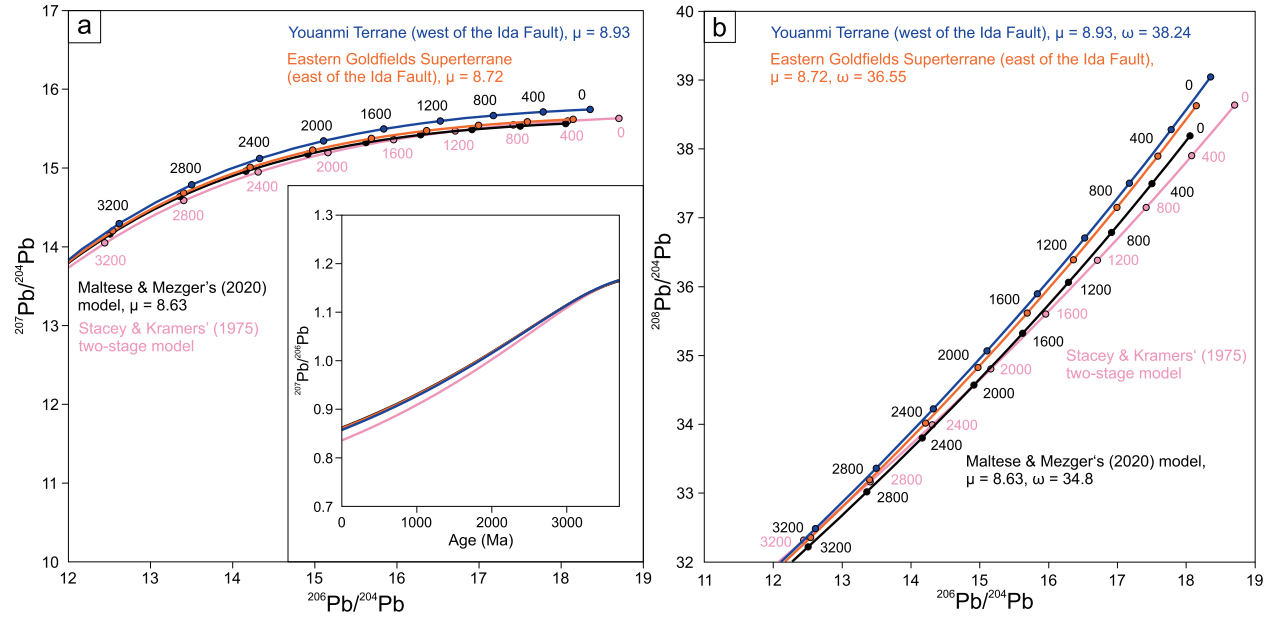

Fig. 7. a) Pb growth curves for uranogenic common Pb in the Yilgarn Craton and $^{207}Pb/^{206}Pb$ vs. age curves for common Pb correction as inset to the bottom right. The growth curve plotted after equations Eq. (4) and Eq. (5) describes the evolution of uranogenic common Pb in the Youanmi Terrane west of the Ida Fault (blue). The growth curve plotted after equations Eq. (7) and Eq. (8) describes the evolution of uranogenic common Pb in the Eastern Goldfields Superterrane east of the Ida Fault (orange). The blue and orange curves are based upon the start date (4498 Ma) and initial Pb composition after Maltese & Mezger (2020) and average μ values for either side of the Ida Fault calculated in this study. Growth curves after Maltese & Mezger (2020; black) and Stacey & Kramers (1975; pink) are plotted for comparison. The four Pb evolution curves mostly overlap before ~3400 Ma but differ significantly in the interval between ~3400 and 0 Ma. Black ages refer to the curves for the Yilgarn Craton and Maltese & Mezger's (2020) growth curve, pink ages refer to Stacey & Kramers' (1975) growth curve. b) The blue growth curve plotted after equations Eq. (4) and Eq. (6) describes the evolution of thorogenic common Pb in the Youanmi Terrane and the orange curve plotted after equations Eq. (7) and Eq. (9) the evolution of thorogenic common Pb in the Eastern Goldfields Superterrane. In an analogous manner to the graphs for uranogenic common Pb, the calculation of the growth curves is based upon the start date (4498 Ma) and initial Pb composition after Maltese & Mezger (2020) and average μ and ω values for either side of the Ida Fault calculated in this study. The recent $^{238}U/^{235}U$ ratio of 137.818 after Hiess et al. (2012) was used for the calculation of all curves. (For interpretation of the references to colour in this figure legend, the reader is referred to the web version of this article.)

the Pb evolution on the scale of the Yilgarn Craton. The Ida Fault – a major crustal-scale boundary – is discernible in our K-feldspar common Pb isotopic data. We documented differences in the median μ values of the samples between west and east of the Ida Fault (Figs. 5 and 6). The average μ of all individual samples is 8.93 ± 0.11 west of the Ida Fault, and higher than the average μ of 8.72 ± 0.12 east of the Ida Fault. An identical trend is observed in average ω with 38.24 ± 1.19 for the Youanmi Terrane and 36.55 ± 1.02 for the EGST. Using Maltese & Mezger's (2020) framework and adjusting the μ and ω value yields the following equations for Pb evolution in the Yilgarn Craton:

For the more crustal Youanmi Terrane in the western Yilgarn Craton:

$$\frac{^{206}Pb}{^{204}Pb} = 9.345 + 8.93 \times \left(e^{\lambda_x 4.498Ga} - e^{\lambda_x t_2}\right) \quad (4)$$

$$\frac{^{207}Pb}{^{204}Pb} = 10.37 + \frac{8.93}{137.818} \times \left(e^{\lambda_y 4.498Ga} - e^{\lambda_y t_2}\right) \quad (5)$$

$$\frac{^{208}Pb}{^{204}Pb} = 29.51 + 38.24 \times \left(e^{\lambda_z 4.498Ga} - e^{\lambda_z t_2}\right) \quad (6)$$

For the more juvenile Eastern Goldfields Superterrane in the eastern Yilgarn Craton:

$$\frac{^{206}Pb}{^{204}Pb} = 9.345 + 8.72 \times \left(e^{\lambda_x 4.498Ga} - e^{\lambda_x t_2}\right) \quad (7)$$

$$\frac{^{207}Pb}{^{204}Pb} = 10.37 + \frac{8.72}{137.818} \times \left(e^{\lambda_y 4.498Ga} - e^{\lambda_y t_2}\right) \quad (8)$$

$$\frac{^{208}Pb}{^{204}Pb} = 29.51 + 36.55 \times \left(e^{\lambda_z 4.498Ga} - e^{\lambda_z t_2}\right) \quad (9)$$

A $^{207}Pb/^{206}Pb$ vs. age plot for the different Pb models is given as an inset on Fig. 7. The Pb evolution curves can be well approximated by the following 4th order polynomial functions, which provide a means to easily calculate model $^{207}Pb/^{206}Pb$:

Youanmi Terrane – west of the Ida Fault (blue curve):

$$y = 0.854 + 9.392 \times 10^{-5}x - 3.957 \times 10^{-8}x^2 + 2.362 \times 10^{-11}x^3 - 3.688 \times 10^{-15}x^4 \quad (10)$$

EGST – east of the Ida Fault (orange curve):

$$y = 0.857 + 9.250 \times 10^{-5}x - 3.840 \times 10^{-8}x^2 + 2.301 \times 10^{-11}x^3 - 3.602 \times 10^{-15}x^4 \quad (11)$$

In order to test the effect of different Pb evolution models on common Pb corrections in U-Th-Pb geochronology, we calculate the influence of our novel Yilgarn Craton Pb evolution models on corrected U-Pb ages for a range of

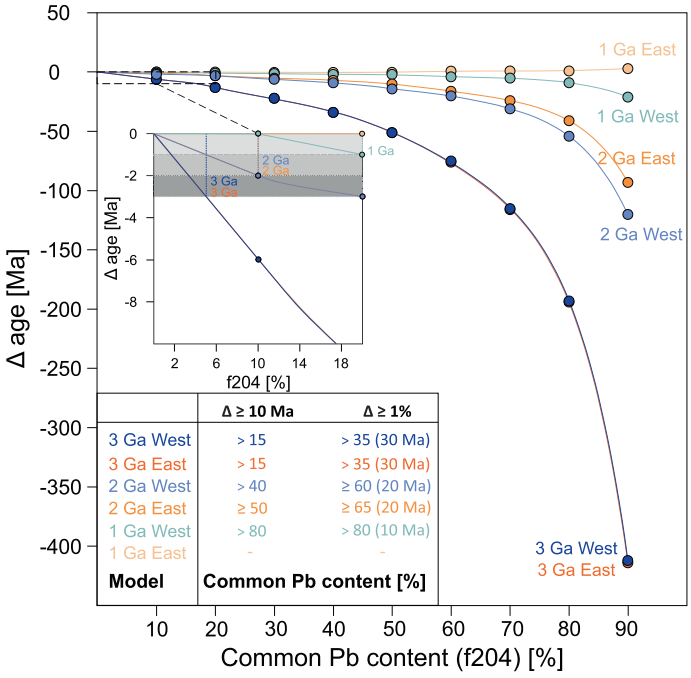

Fig. 8. Influence of the novel Pb evolution models for the Yilgarn Craton on $\Delta^{207}Pb/^{206}Pb$ ages in common Pb correction. The age difference of the Yilgarn Craton models relative to Stacey & Kramers' (1975) model for different concordant model sample ages (1 Ga, 2 Ga, and 3 Ga) is plotted versus different common Pb contents (data points from 10% f204 up to 90% f204). The approximate common Pb threshold values for Δcorrection ≥ 10 Ma and ≥ 1% illustrate that common Pb correction becomes rapidly more model-dependent with high common Pb contents – especially for older sample ages. The difference between the two novel Pb evolution models for the Yilgarn Craton, on the other hand, is smaller for older sample ages. The novel models can provide significantly better accuracy for high-precision analysis techniques like TIMS (see inset). Three grey bars on the inset display the average uncertainty of a TIMS analysis (= 0.1%) for three different sample ages: 1 Ga (uncertainty = 1 Ma), 2 Ga (uncertainty = 2 Ma), 3 Ga (uncertainty = 3 Ma). The lower intersection of each Pb evolution model curve and the uncertainty bars flags the minimum common Pb fraction for which application of our novel Yilgarn Craton Pb models is statistically significant.

different ages and magnitudes of common Pb. We reference corrected U-Pb ages to Stacey & Kramers' (1975) two-stage model. Accordingly, we calculate the difference in corrected age for three different sample ages (1 Ga, 2 Ga, and 3 Ga) and for common Pb contents of 0% up to 90% in steps of 10% (Fig. 8).

The uncertainty of many analytical U-Pb ages is in the range of ± 10 Ma (see e.g., Schoene, 2014, and Schaltegger et al., 2015, for reviews of the U-Th-Pb analysis techniques). Typical average age uncertainties of Secondary Ion Mass Spectrometry (SIMS) U-Pb analyses are ~1.5% and ~2% for LA-ICPMS U-Pb (Schoene, 2014). Hence, we consider a difference in common Pb correction, using the different Pb evolution models, of greater than 10 Ma to be significant. Application of the novel Yilgarn Craton Pb evolution models becomes increasingly significant with older sample ages (Fig. 8). Furthermore, common Pb correction rapidly becomes more model-dependent for samples with higher common Pb contents (Fig. 8). Only at very high common Pb contents for the 1 Ga and 2 Ga ages do age corrections exceed 10 Ma relative to Stacey & Kramers' (1975) model. For a 3 Ga sample a ≥ 10 Ma age difference is seen for samples with approximately > 15% common Pb after both novel Yilgarn Craton models. Such high common Pb contents would be unusual for the majority of U-Th-Pb geochronology applications and it is clear that a model-based common Pb correction can induce a systematic error when using minerals with high common Pb contents. Nonetheless, these results provide a quantification of the magnitude of the induced uncertainty in common Pb correction due to the common Pb model choice.

Analytical advances in mass spectrometry will inevitably lead to an increasing need for more accurate common Pb correction. The new Pb evolution models are most pertinent to high-precision geochronology such as thermal ionization mass spectrometry (TIMS) of old material but of less concern for lower precision U-Pb geochronology where the magnitude of the difference in common Pb correction is less than the typical analytical precision (see inset on Fig. 8). Average age uncertainties for measurements using TIMS can be as low as ~0.1% (Schoene, 2014; Schaltegger et al., 2015). The shaded bars on the inset on Fig. 8 represent the average uncertainty of a TIMS measurement for 1 Ga, 2 Ga, and 3 Ga samples. The lower intersections of the grey bars with our Yilgarn Craton Pb evolution model curves define the maximum common Pb content a sample of a specific age can have beyond which the error associated with the common Pb model is greater than analytical uncertainty. A correction age difference greater than the average TIMS analysis uncertainty is seen for 1 Ga samples from the Youanmi Terrane with ≥ 20% common Pb. In contrast, the common Pb content of 1 Ga EGST samples must be ≥ 60% for the age correction difference to be greater than average analysis uncertainty of ≥ 0.1% (1 Ma). For 2 Ga samples the Pb model curves for the Youanmi Terrane and the EGST both intersect the TIMS uncertainty bar at 10% common Pb. However, in the case of 3 Ga samples both Yilgarn Craton Pb models indicate a difference in age correction greater than TIMS uncertainty of 0.1% when the common Pb fraction is ≥ ~5%. This lower relevance threshold underpins the importance of Pb models in common Pb correction for Archean samples used in high-precision geochronology.

7.3. Fractionation, source tracking, and geochemistry patterns in the Yilgarn Craton

Numerous Lu-Hf (Mole et al., 2014, 2019) and Sm-Nd (e.g., Champion & Sheraton, 1997; Cassidy & Champion, 2004; Champion & Cassidy, 2007; Champion, 2013; Mole et al., 2013) isotopic studies and resultant maps, as well as the spatial and temporal distribution of granite crystallization ages (e.g., Mole et al., 2012) have elucidated the crustal structure of the Yilgarn Craton. The Lu-Hf and Sm-Nd isotopic patterns in granites reflect the geochemistry of their bulk source. Hf and Nd model ages from granites are typically interpreted to estimate the average source age and may track some fundamental deep mantle fractionation process (Champion, 2013). Hf and Nd model age maps show clear distinctions between older model ages in the Youanmi Terrane versus younger model ages in the EGST (Fig. 1a). The accurate approximation of the Yilgarn Craton's Pb evolution through Maltese & Mezger's (2020) model for the Bulk Silicate Earth is surprising, as it implies single-stage Pb evolution starting at 4.498 Ga. Nd and Hf isotopic data on the other hand, reveal multiple mantle input events between 3.0 and 2.7 Ga (e.g., Mole et al., 2019).

The production of granitic melts is a process that typically occurs in the mid to lower crust (e.g., Barbarin, 1990). The mineral assemblage of granitic rocks relates to magma composition and conditions of crystallization. Magma composition will depend on a variety of different factors including melting source (from the crust or the mantle), crystal fractionation processes and conditions, melt contamination or a mixture of these factors (e.g., Miller et al., 1990; Barbarin, 1999). The derivative parameters μ and ω of the Pb isotopic system inform on Pb source reservoirs. Differences in average μ and ω values between west and east of the Ida Fault, whilst subtle (Figs. 5 and 6), are not temporally controlled (see appendix K; figures K.1a and K.1b). The oldest sample population in our transect is from the Youanmi Terrane, has elevated median μ and ω values, and ranges in crystallization age from 2712 to 2671 Ma. This higher-μ and higher-ω granite suite is postdated by lower-μ and lower-ω EGST granites (excluding samples 92969113A and 2001969122 which are discussed below) that crystallized between 2665 Ma and 2640 Ma (Table 3). The two samples with the youngest crystallization ages in the sample set (99967114 and 98969019) were taken in the Youanmi Terrane and have higher μ and ω values relative to the samples from east of the Ida Fault with older crystallization ages (appendix K; figures K.1a and K.1b). The differences in μ and ω indicate dissimilarity in the bulk U/Pb and Th/Pb ratio of the source. Such a Pb isotopic pattern is consistent with Nd and Hf model ages in the Yilgarn Craton (Figs. 1a, 4 and 9). The common Pb isotopic signature in K-feldspar implies either a timing difference in source component extraction – analogous to the Nd and Hf isotope system – or that the

Table 3
Geochemistry of the granite samples.

Geoscience Australia (GA) Sample ID	Granite age [Ma] (Age reference)	± 95% conf. [Ma]	Median μ	Median ω	Median κ	Fe-number	n_{elem}	Median ^{238}U conc. [ppm]	Median ^{232}Th conc. [ppm]	Nd model age [Ma]
West of the Ida Fault										
99967114	2630 (B)	50	8.93	39.01	4.36	0.7	42	0	0	3210
98969045	2700 (A)	15	8.86	37.42	4.23	0.68	40	5.25E−04	0	2960
98969033	2671 (A)	3	9.04	39.27	4.34	0.68	32	0	0	3290
98969055	2712 (A)	6	8.84	36.49	4.12	0.68	32	0	0	3240
97969063	2684 (A)	8	8.80	37.56	4.26	0.75	40	1.82E−02	5.44E−02	3330
97969082A	2682 (A)	5	8.93	38.71	4.34	0.67	40	2.82E−03	1.13E−04	3320
98969019	2640 (B)	50	9.12	39.98	4.41	0.86	44	1.08E−02	1.10E−02	3160
East of the Ida Fault										
92969068	2640 (E)		8.79	38.04	4.33	0.82	40	8.64E−03	4.59E−04	3280
92969054	2640 (E)		8.73	36.18	4.14	0.72	48	1.98E−02	7.55E−04	3080
92969082	2665 (D)	5	8.85	37.42	4.22	0.75	11	0	0	2910
92969071	2650 (E)		8.77	36.57	4.16	0.89	0	–	–	3110
92969052	2650 (E)		8.78	37.02	4.22	0.76	36	2.70E−03	6.04E−03	3050
2001969108	2650 (E)		8.63	35.96	4.17	0.74	42	7.99E−03	0	2870
2001969113	2640 (E)		8.48	34.65	4.08	0.76	42	7.92E−03	0	2870
2001969122	2939 (C)	6	9.64	39.81	4.12	0.78	39	8.93E−03	7.73E−04	3130
92969113A	2671 (D)	12	8.49	34.85	4.11	0.87	41	1.36E−02	0	3010

Granite age references: (A) = U-Pb SHRIMP zircon date in Fletcher & McNaughton (2001); (B) = Geoscience Australia estimate, based on U-Pb SHRIMP zircon data presented by Fletcher & McNaughton (2001); (C) = U-Pb SHRIMP zircon date in Dunphy et al. (2003); (D) = New U-Pb SHRIMP zircon data presented herein; (E) = Estimated; no U-Pb zircon data available.
Median μ: Median μ value of the sample based upon the mean of μ_{206} and μ_{207} for each individual group A and B data point calculated after Eq. (D.1) and Eq. (D.2).
Median ω: Median ω value of the sample based upon individual group A and B data points calculated after Eq. (D.3).
Median κ: Median κ value of the sample based upon individual group A and B data points calculated after Eq. (D.4).
N_{elem}: Number of spots analyzed for ^{238}U and ^{232}Th concentrations.
Median ^{238}U conc. [ppm]: ^{238}U concentration of all spots analyzed for element concentrations; note: we calculated with 0 ppm for analyses below detection limit.
Median ^{232}Th conc. [ppm]: ^{232}Th concentration of all spots analyzed for element concentrations; note: we calculated with 0 ppm for analyses below detection limit.

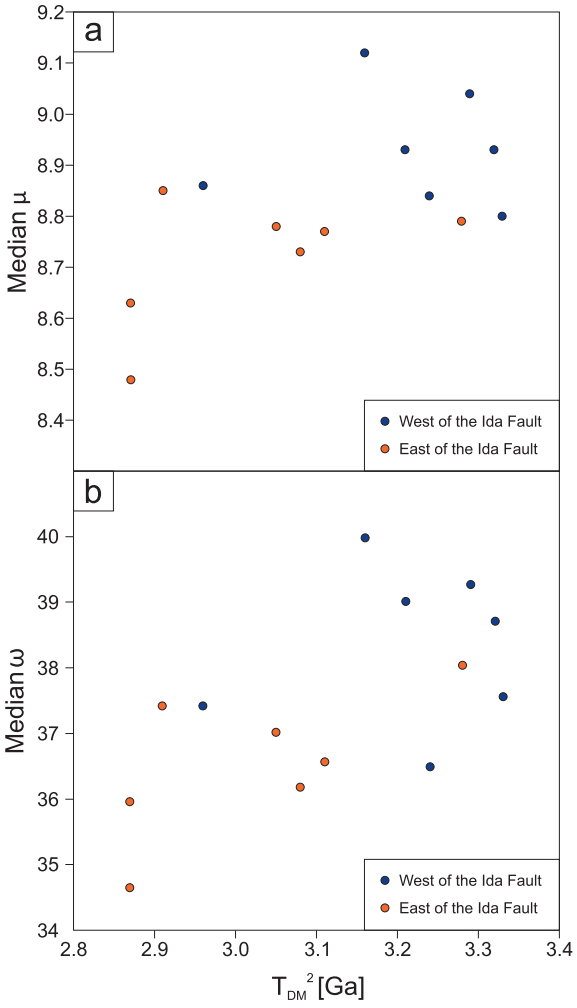

Fig. 9. Comparison of Pb isotope derivative parameters and Nd model ages. Median μ (a; Eq. (D.1) and Eq. (D.2)) and median ω (b; Eq. (D.3)) are plotted in relation to the two-stage Nd model age T_{DM}^2. Samples from the older and probably more crustal Youanmi Terrane form a higher-median-μ/higher-median-ω and older Nd model age cluster. Samples from the Eastern Goldfields Superterrane have lower median μ and median ω values and younger Nd model ages. The two samples 92969113A and 2001969122 are excluded from this figure because the K-feldspar signature in the samples, and thus also the μ and ω values, are interpreted to have been affected by metamorphism.

granitic rocks west of the Ida Fault were derived from a bulk source containing a higher proportion of preexisting crustal material with elevated U/Pb and Th/Pb ratio relative to those in the EGST. Granites from the EGST have less evolved Nd and Hf isotopic signatures relative to those in the Youanmi Terrane and have, on average, a lower μ and ω source (Figs. 4 and 9).

It is interesting that there is also a difference in average κ, and thus in source Th/U, between west and east of the Ida Fault (Fig. 6), which is somewhat unexpected as U and Th both are lithophile elements and potentially fractionate into the crust to a very similar relative extent. Differing average κ values may document timing differences in initial source crust-mantle fractionation events. The subtle difference in κ might also reflect source age variation across the Ida Fault as implied in Nd and Hf data that is not accounted for in single-stage Pb evolution models.

The vast majority of our data from samples taken on either side of the Ida Fault correspond with a 'triangular' Pb source compositional domain as proposed by McNaughton & Groves (1996) for the Yilgarn Craton. According to their model, this isotopic pattern suggests both upper crust and depleted mafic crust as the main Pb sources. As illustrated in Fig. 5a there is a general deficit in radiogenic ^{206}Pb in relation to the global galena reference line after Albarède & Juteau (1984). This deficit in ^{206}Pb can be interpreted as either a reflection of greater mantle Pb or enrichment with ancient crustal Pb (Hofmann, 1997; Milot et al., 2021). Specifically, the ^{206}Pb deficit is less in the Youanmi Terrane samples, consistent with a greater mantle contribution in EGST samples (Fig. 5a). $^{207}Pb/^{204}Pb$ ratios reveal an opposite trend of general ^{207}Pb enrichment with respect to the global galena reference line (Fig. 5b). Radiogenic ^{208}Pb appears enriched in Youanmi Terrane samples, while EGST samples align closely with the galena linearization, similar to the trends in uranogenic common Pb (Fig. 5c). Negative correlations between granite crystallization ages and $^{206}Pb/^{204}Pb$, $^{207}Pb/^{204}Pb$, $^{208}Pb/^{204}Pb$ ratios in Youanmi Terrane samples (Fig. 5) imply increasing crustal influence with time in Youanmi Terrane granites. The EGST Pb arrays in inverse space imply greater mantle contribution in a restricted temporal window that contrasts with greater crustal contributions that evolve through time in the Youanmi Terrane. Such patterns in a simple geodynamic context may reflect dominantly extensional processes in the EGST (Czarnota et al., 2010) synchronous with progressive crustal reworking of the Youanmi Terrane.

Granite geochemical parameters track the magma source, melting conditions, and possible melt contamination, as well as the differentiation history of the silicate liquid. For example, Fe-number distinguishes between ferroan granitic rocks defined by a higher Fe-number and magnesian granitic rocks defined by a lower Fe-number, with this boundary being SiO_2-dependent (Frost et al., 2001; Frost & Frost, 2008). The enrichment in Fe in ferroan granites is often interpreted to be related to the differentiation history of the granitic melt and to indicate a likely derivation from higher-temperature and/or more reduced mafic magmas such as alkali basalts or tholeiites (Frost & Frost, 1997; Frost et al., 2001).

Higher Fe-numbers appear more frequently in samples from east of the Ida Fault (Fig. 10), suggesting dissimilarity in the differentiation paths between the Youanmi Terrane and EGST. The higher Fe-numbers in the more juvenile EGST possibly reflect stronger granite differentiation and partial melting of basaltic rocks in the EGST relative to the Youanmi Terrane (Miyashiro, 1974; Frost et al., 2001; Frost & Frost, 2008). Enrichment in Fe can also result from crustal melting under dryer conditions at higher temperatures (Collins et al., 1982). However, multi-isotope (Nd, Hf, Pb) evidence suggests a more juvenile bulk source for the EGST. The greater magnesian character on average for Youanmi Terrane granitic rocks may indicate that these

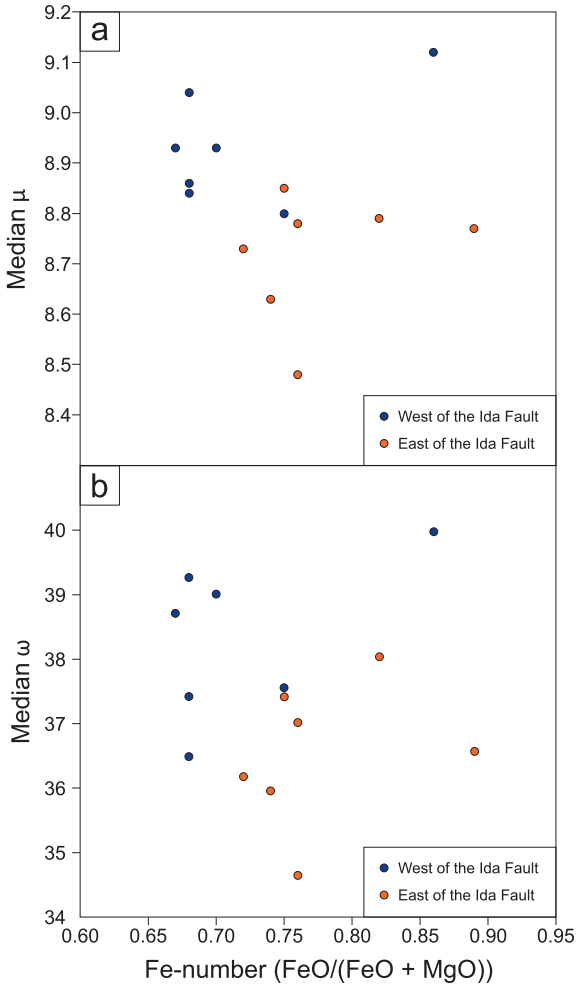

Fig. 10. Geochemistry of the granite samples. Median μ (a; Eq. (D.1) and Eq. (D.2)) and median ω (b; Eq. (D.3)) are plotted in relation to the geochemical parameter Fe-number. The parameter Fe-number (FeO/(FeO + MgO)) after Frost et al. (2001) is utilized in geochemistry to classify granitic rocks. The more magnesian (lower Fe-number) granitic rocks west of the Ida Fault correspond with higher median μ and ω values and the more ferroan (higher Fe-number) granitic rocks east of the Ida Fault correspond with lower median μ and ω values. Two outlier data points with the highest Fe-number values can be explained by unusual geochemistry compared to the other samples (very low MgO content). The two samples 92969113A and 2001969122 are excluded from this figure because the K-feldspar signature in the samples, and thus also the μ and ω values, are interpreted to have been affected by metamorphism.

magmas followed a more oxidizing differentiation path than the EGST magmas (Frost et al., 2001). Generally, Fe-number shows a positive correlation with SiO_2 in the vast majority of magmas – independent of crystallization time and location (e.g., Miyashiro, 1974; Cox et al., 1979; Frost et al., 2001; Arculus, 2003). As expected, over the entire Yilgarn Craton magmas from both the Youanmi Terrane and EGST show a weak positive trend to higher Fe-number with increasing SiO_2 content (Appendix L; figure L.1). In the sample set with Pb isotope data (over a more limited SiO_2 range of ~71–75 wt%), no clear correlation is apparent between SiO_2 and μ and ω (Appendix L; figures L.2 and L.3). Linear regression of twelve of fourteen K-feldspar μ values (excluding samples 98969019 and 92969071 with the lowest MgO content and highest Fe-number values) versus Fe-numbers indicates an apparent negative relationship ($p = 0.069$ [93.1% conf.], $r^2 = 0.29$; Fig. 10a).

Given the Yilgarn-wide relationship between Fe-number and SiO_2 content (Appendix L; figure L.1), and the relationship between Fe-number and μ and ω in our samples, one may predict higher μ and ω with lower SiO_2, when considered over sufficient compositional range. A possible implication of such a relationship could be that higher μ and ω, lower Fe-number, and higher SiO_2 in the Youanmi Terrane granites result from either a more primitive protolith or higher degrees of partial melting.

Given the relatively small variations between average μ and ω values from west and east of the Ida Fault, K-feldspar Pb isotopes rather subtly resolve a distinction between the Youanmi Terrane and EGST. The majority of uranogenic and thorogenic common Pb isotopic data acquired in this study plots above the Pb evolution curve for the Bulk Silicate Earth (Fig. 3). The inference of this observation is that there must have been differentiation, probably related to craton-building magma input events. Three lines of evidence suggest that U-Pb fractionation related to granite production, as tracked by K-feldspar, is an influence, in addition to crust-mantle fractionation, on the isotopic signal of felsic crust: 1) Using granite as the sampling medium favors the more fractionated, felsic end-member of the source and confines the sampled range of source μ and ω values. 2) With the exception of two samples 92969113A and 2001969122 interpreted as metamorphic, samples in this study represent a granite bloom between ~2712 and 2630 Ma and resolve a time difference of less than 100 Ma and thus have had little time for source differentiation and isotopic ingrowth. 3) The apparent negative correlation of source μ and ω with Fe-number and the possible connection of iron- or magnesium-enriching processes to the Pb isotopic pattern indicates a positive relationship between granite production processes and Pb isotopic value. Thus, differentiation paths appear to differ in granites from west and east of the Ida Fault. 4) $^{206}Pb/^{204}Pb$, $^{207}Pb/^{204}Pb$, and $^{208}Pb/^{204}Pb$ ratios of Youanmi Terrane samples plotted in inverted Pb space (Fig. 5) reveal a greater crustal source in younger samples from the Youanmi Terrane. Accordingly, Pb isotopes in granite K-feldspar most likely visualize differing degrees of crustal contamination as a secondary signal.

The genesis of ore deposits through hydrothermal fluid flow influences Pb isotopic signals in the mid to upper crust (Doe & Stacey, 1974). Huston et al. (2005, 2014) interpreted Pb ore low-μ zones of the EGST as reflecting an extensional setting and – analogous to Sm-Nd data and our results from Pb isotopes in granite K-feldspar – indicating greater mantle input relative to the Youanmi Terrane. Correlations between Pb isotopes from Pb-rich ores and Nd data in the Yilgarn Craton are also documented in the studies of Browning et al. (1987) and Champion & Huston (2016).

Despite the narrow age and limited source compositional range, information on the U/Pb and Th/Pb ratio of the source is still remarkably well recovered in the K-feldspar Pb isotopic data, which strengthens the concept of this system as a source tracking tool. The similarity of Pb to both Nd and Hf isotopic signatures implies that some source signal is retained within the common Pb system that originated from extraction of crustal material out of the mantle. Thus, our data indicate that, as with Nd- and Hf-isotopic studies, Pb isotopes can trace distinct geological processes on either side of craton-scale boundaries like the Ida Fault (Carignan et al., 1993). These geochemical boundaries can typically be linked with known or geophysically inferred tectonic boundaries. Furthermore, chemical communication between the deep crust and the upper crust is also suggested by the similar pattern in common Pb isotopes from K-feldspar in granite and upper crustal Pb ores (Browning et al., 1987; Huston et al., 2005; Huston et al., 2014; Champion & Huston, 2016). Hence, our new results illustrate the full crustal column transfer of an initially deep basement signature. Whilst the Pb isotopic signature in granite K-feldspar may be blurred by fractionation related to granite formation in the mid to lower crust, an original signal nonetheless remains visible in Pb-rich ores of the upper crust. Thus, a distinct upper crust of the Yilgarn Craton was not emplaced on top of the lower crust. Our results rather suggest a common source for the entire lithospheric section. This study underlines the value of combining different isotopic systems to unravel the complex structure of Earth's continental crust. Pb isotopic data in granite K-feldspar are potentially easier to obtain in large numbers compared to other isotopic systems, given both the mineral's ubiquity in felsic crust and its general ease of analysis, and accordingly, may represent an efficient crustal evolution mapping tool.

In spite of the simplifying assumption of single-stage Pb evolution starting at 4.498 Ga, Maltese & Mezger's (2020) model appears effective for the Yilgarn Craton. This is indicated by the geochemical fingerprinting of differences in μ and ω across the Ida Fault (Fig. 6) together with the correspondence of Pb isotopic signatures with Nd and Hf signatures (Figs. 4 and 9), and the good reproduction of U-Pb granite crystallization ages (Table 2).

7.4. Case studies

7.4.1. Altered sample

The samples of this transect that do not fall on paleogeochrons for the known granite crystallization age provide useful case studies to evaluate secondary processes that may influence Pb isotopic signatures.

Sample 99967114 is a feldspar-porphyritic, fine-grained biotite granodiorite. It was taken close to greisen-related tin mineralization. Rare to minor thin quartz veins and pegmatites cut the granodiorite.

Pb isotopic data of sample 99967114 scatter towards present-day Pb model compositions even after filtering (compare individual common Pb plot in appendix I). Radiogenic ingrowth, potentially from U-bearing micro-inclusions, is interpreted to influence the young end of this scattered array. This underlines that the calculated Pb model age for this sample does not have any geological meaning. The least radiogenic data points overlap the paleogeochron for the U-Pb age of the granite. Filtering led to the removal of 28 data points in group C with elevated Hg content ($^{204}Hg/^{204}Total \geq 5\%$). The average Pb content of K-feldspar grains measured in sample 99967114 is comparatively low. 13 of the analyzed data points in this sample have an approximated Pb content of less than 10 ppm. The likely Pb loss or Pb mixing indicated by the large number of low-Pb-data in addition to the high portion of Hg and moderate petrological signs of alteration in the K-feldspar in this sample suggests that the granite has been affected by alteration consistent with the scatter in data preventing calculation of a Pb model age. This sample demonstrates the importance of filtering Pb isotopic data for Hg and Pb content.

7.4.2. Metamorphic samples

An examination of the U-Pb zircon geochronology of samples 92969113A and 2001969122 identifies complexities in these samples from east of the Ida Fault. All data in both samples show a significantly elevated Hg content ($^{204}Hg/^{204}Total \geq 5\%$ in all cases).

Data points of 92969113A and 2001969122 form a linear array that is distinctly offset from the main trend in $^{207}Pb/^{204}Pb$ vs. $^{206}Pb/^{204}Pb$ space (Fig. 3a). The Pb model ages do not correspond to the currently interpreted U-Pb zircon crystallization ages. However, group A and B data of both samples 92969113A and 2001969122 fall on a linear trend that implies a model age of c. 2770 Ma. Data of sample 92969113A also form a separate trend in $^{208}Pb/^{204}Pb$ vs. $^{206}Pb/^{204}Pb$ space that is ~100 Ma older in relation to the Pb evolution models of Stacey & Kramers (1975) and Maltese & Mezger (2020) (Fig. 3b).

Sample 92969113A is a gneissic, porphyritic, high-Ca, biotite (meta)granite (Table 1). U-Pb SHRIMP zircon data for this sample are documented in appendices A and B. Only five out of 32 U-Pb zircon analyses define an apparent magmatic crystallization age of 2671 ± 12 Ma (95% conf.; MSWD = 1.3; probability = 0.29) for the igneous precursor of the gneiss. A group of five analyses is interpreted to represent pre-2800 Ma inheritance, of which one analysis has a $^{207}Pb/^{206}Pb$ date as old as 2941 Ma.

Sample 2001969122 is a foliated and lineated, incipiently banded, high-Ca, fine- to medium-grained biotite granodiorite to granitic gneiss (Table 1) with dominant feldspar (plagioclase > K-feldspar), quartz, and biotite (Dunphy et al., 2003). A zircon population (n = 13) with visible cores, zoning and small inclusions, was utilized to calculate an interpreted U-Pb crystallization age of 2939 ± 6 Ma for the granitic rock (Dunphy et al., 2003). Weak and blurred zoning in some of the grains hints at partial recrystallization.

Equations after Albarède et al. (2012) yield a Pb model age of 2774 Ma for sample 2001969122, which is more than 150 Ma younger than the calculated zircon U-Pb crystallization age (Figs. 2 and 3), and a Pb model age of 2772 Ma for sample 92969113A (Table 2).

Given (i) pre-2.9 Ga U-Pb analyses in both samples 92969113A and 2001969122, and (ii) their distinct $^{207}Pb/^{204}Pb$ vs. $^{206}Pb/^{204}Pb$ trend (Fig. 3a), we interpret the Pb isotopes in K-feldspar from these two samples to reflect metamorphism along the terrane boundary between the Kurnalpi and Burtville terranes after the initial > 2.9 Ga granite emplacement. Isotopic data indicate that the Burtville Terrane may have a history that reaches back to the Mesoarchean (Pawley et al., 2012), and is therefore older than the Kurnalpi Terrane. The metamorphism was probably characterized by migmatization and recrystallization of the granites. The gneissic character of both granodiorite samples underlines that recrystallization during metamorphism is likely. In addition, the geochemistry of the two samples is distinct; for instance, the chemical alteration indices (Nesbitt & Young, 1982) are elevated relative to all the other samples. The weak zoning in the zircon crystals is another indicator of recrystallization. Inducing a second stage of Pb evolution starting from the interpreted crystallization age of approximately 2940 Ma, that intersects the Pb evolution model after Maltese & Mezger (2020) at ~2670 Ma (the youngest crystallization age indicated by U-Pb data points), requires lower μ values, and thus a lower uranium content in the source; the adjusted μ values for the second stage are ~5 and indicate rejuvenation during a metamorphic overprint (Gancarz & Wasserburg, 1977).

Our Pb isotope signatures from migmatization-related K-feldspar reveal the effect of metamorphism, as the separate linear array in the $^{207}Pb/^{204}Pb$ vs. $^{206}Pb/^{204}Pb$ plot does not correspond to the crystallization ages. The calculated Pb model age cannot be interpreted as representing the exact timing of metamorphism, as the Pb isotopic signature reflects mixing. The apparent Pb model age of 2670 Ma is not the crystallization age of sample 92969113A. It is best interpreted as reflecting recrystallization of the original magmatic K-feldspar during metamorphism, and consequently incomplete resetting of the Pb signature in K-feldspar. We conclude that our data are consistent with an overprinting event between the U-Pb granite crystallization ages of c. 2940 Ma and c. 2670 Ma. This age constraint overlaps with periods of metamorphism identified by Browning et al. (1987) for the EGST and by Binns et al. (1976), Goscombe et al. (2009), and Jones et al. (2021) for this particular region. The highest metamorphic degrees in the EGST can typically be found around granite domes (e.g., Binns et al., 1976; Jones et al., 2021). Rejuvenation of Burtville Terrane crust between c. 2940 Ma and 2755 Ma and at c. 2720 Ma also matches the interpreted overprint time frame (Pawley et al., 2012).

7.4.3. Calculation, interpretation, and applications of Pb-in-K-feldspar model ages

Pb model ages presented in this study are based on an effective model assuming single-stage Pb evolution. Zartman & Wasserburg (1969) demonstrated that model ages deduced from Pb isotopes in K-feldspar – using Houtermans' (1946) model – approximate radiometric ages with an average standard deviation of ± 120 Ma in non-metamorphic or slightly metamorphic samples. Our results suggest that model ages yielded by Pb isotopes in granite K-feldspar calculated after Albarède et al. (2012) can be in good agreement with zircon U-Pb granite crystallization ages under the conditions that there is no isobaric overlap of Hg on Pb, negligible U in K-feldspar grains, and the Pb evolution model is appropriate. Granite K-feldspar Pb isotopes provide important source context which in turn can help refine geochronology interpretations (e.g., granites with large inherited zircon loads). Consequently, the method proves useful in resolving complexities in accessory mineral geochronology via distinguishing between inherited, magmatic, or metamorphic zircon, relative to major phase silicate growth. Pb isotopes in K-feldspar clearly cannot replace U-Pb zircon geochronology as a geochronometer but nonetheless complement this tool.

8. CONCLUSIONS

Based on comparisons between known granite crystallization ages and K-feldspar Pb model ages, Maltese & Mezger's (2020) Pb evolution framework is more suitable for the Yilgarn Craton than Stacey & Kramers' (1975) two-stage evolution model. This finding is pertinent to studies that characterize Pb source compositions and important, since the latter has been widely utilized for common Pb correction in geochronology over decades in this region.

We documented differences in K-feldspar average μ and ω between west and east of the major Ida Fault, with the average μ and ω values higher in samples from west of the Ida Fault. We derive new equations that describe the Pb evolution in the Yilgarn Craton using Maltese & Mezger's (2020) Pb evolution model as a framework and calculated average μ and ω values for the Youanmi Terrane west of the Ida Fault ($\mu = 8.93 \pm 0.11$; $\omega = 38.24 \pm 1.19$) and the Eastern Goldfields Superterrane east of the Ida Fault ($\mu = 8.72 \pm 0.12$; $\omega = 36.55 \pm 1.02$). Common Pb corrected U-Pb ages after these novel Yilgarn Pb evolution models are significantly different compared to ages corrected after Stacey & Kramers (1975) for Archean samples measured with high precision, when common Pb is ≥ ~5%.

The differences in average μ and ω between an older Youanmi Terrane built up on a higher proportion of preexisting crustal material relative to a more juvenile, younger Eastern Goldfields Superterrane, document similar trends to that recorded in Sm-Nd and Lu-Hf isotopic systems. A combination of our results with Pb isotopic data from Pb-rich ores reveals that Pb isotopes document chemical communication between the mid to lower crust and the upper crust. Whilst the age and compositional range of the investigated samples is limited and the initial isotopic signature that stems from a mantle source fractionation event may be blurred through granite fractionation processes it is, nonetheless, still visible. The large-scale implication is that the legacy of the original deep basement signature is transported in Pb isotopic data all the way through the crust from the mantle to upper crustal systems.

Where Pb isotope ratios are not affected by isobaric interference, the feldspar has negligible U content, and an effective Pb evolution model is available, Pb isotopes in granite K-feldspar can aid in resolving complexities in zircon geochronology. K-feldspar Pb isotopes help distinguish

between metamorphic and magmatic zircon growth and unravel the relationship to major phase silicate growth by providing valuable source information.

Declaration of Competing Interest

The authors declare that they have no known competing financial interests or personal relationships that could have appeared to influence the work reported in this paper.

ACKNOWLEDGEMENTS

This project was funded by Australian Research Council Linkage grant LP180100199 between Curtin University, the Geological Survey of Western Australia (GSWA), and Northern Star Resources Ltd. We thank David Huston from Geoscience Australia, whose valuable comments on an earlier draft significantly improved the quality of this manuscript. Bryant Ware is acknowledged for support with sample acquisition. Brad J. McDonald is thanked for technical support with the laser ablation instrumentation. GeoHistory Facility instruments in the John de Laeter Centre (JdLC), Curtin University, were funded via an Australian Geophysical Observing System grant provided to AuScope Pty Ltd. by the AQ44 Australian Education Investment Fund program. Research in the JdLC GeoHistory laser ablation Facility is enabled by AuScope and the Australian Government via the National Collaborative Research Infrastructure Strategy. We thank associate editors Janne Blichert-Toft and Yuri Amelin, as well as Alessandro Maltese and four anonymous reviewers for comprehensive and constructive comments on our work.

APPENDIX A. SUPPLEMENTARY MATERIAL

Supplementary data to this article can be found online at https://doi.org/10.1016/j.gca.2021.11.029.

REFERENCES

Albarède F. and Juteau M. (1984) Unscrambling the lead model ages. *Geochim. Cosmochim. Acta* **48**, 207–212.

Albarède F., Desaulty A.-M. and Blichert-Toft J. (2012) A geological perspective on the use of Pb isotopes in Archaeometry. *Archaeometry* **54**, 853–867.

Andersen T., Elburg M. A. and Magwaza B. N. (2019) Sources of bias in detrital zircon geochronology: Discordance, concealed lead loss and common lead correction. *Earth-Sci. Rev.* **197** 102899.

Arculus R. J. (2003) Use and abuse of the terms calcalkaline and calcalkalic. *J. Petrol.* **44**, 929–935.

Arcuri G. A. and Dickin A. P. (2018) Pb isotope mapping of paleoproterozoic gneisses in the SW Grenville Province: Evidence for a cryptic continental suture. *Geosciences* **8**, 247.

Barbarin B. (1990) Granitoids: main petrogenetic classifications in relation to origin and tectonic setting. *Geol. J.* **25**, 227–238.

Barbarin B. (1999) A review of the relationships between granitoid types, their origins and their geodynamic environments. *Lithos* **46**, 605–626.

Bédard J. H. (2006) A catalytic delamination-driven model for coupled genesis of Archaean crust and sub-continental lithospheric mantle. *Geochim. Cosmochim. Acta* **70**, 1188–1214.

Bédard J. H., Harris L. B. and Thurston P. C. (2013) The hunting of the snArc. *Precambrian Res.* **229**, 20–48.

Binns R. A., Gunthorpe R. J. and Groves D. I. (1976) Metamorphic patterns and development of greenstone belts in the Eastern Yilgarn Block, Western Australia. In *The Early History of the Earth* (ed. B. F. Windley). John Wiley and Sons, pp. 303–313.

Blaxland A. B., Aftalion M. and van Breemen O. (1979) Pb isotopic composition of feldspars from Scottish Caledonian Granites, and the nature of the underlying crust. *Scott. J. Geol.* **15**, 139–151.

Blewett R. S., Henson P. A., Roy I. G., Champion D. C. and Cassidy K. F. (2010) Scale-integrated architecture of a world-class gold mineral system: The Archaean eastern Yilgarn Craton, Western Australia. *Precambrian Res.* **183**, 230–250.

Blichert-Toft J., Delile H., Lee C.-T., Stos-Gale Z., Billström K., Andersen T., Hannu H. and Albarède F. (2016) Large-scale tectonic cycles in Europe revealed by distinct Pb isotope provinces. *Geochem. Geophys. Geosyst.* **17**, 3854–3864.

Browning P., Groves D. I., Blockley J. G. and Rosman K. J. R. (1987) Lead isotope constraints on the age and source of gold mineralization in the Archean Yilgarn Block, Western Australia. *Econ. Geol.* **82**, 971–986.

Carignan J., Gariépy C., Machado N. and Rive M. (1993) Pb isotopic geochemistry of granitoids and gneisses from the late Archean Pontiac and Abitibi Subprovinces of Canada. *Chem. Geol.* **106**, 299–316.

Cassidy K. F. and Champion D. C. (2004) Crustal evolution of the Yilgarn Craton from Nd isotopes and granite geochronology: Implications for metallogeny. In *SEG 2004, Predictive Mineral Discovery Under Cover* (ed. J. R. Muhling). Centre for Global Metallogeny, University of Western Australia, pp. 317–320.

Cassidy K. F., Champion D. C., Krapez B., Barley M. E., Brown S. J. A., Blewett R. S., Groenewald P. B. and Tyler I. M. (2006) A revised geological framework for the Yilgarn Craton, Western Australia. *Geological Survey of Western Australia Record* **2006/8**, 1–8.

Champion D. C. (2013) *Neodymium depleted mantle model age map of Australia: Explanatory notes and user guide*. Geoscience Australia, Canberra.

Champion D. C. and Cassidy K. F. (2002) *Granites in the Leonora-Laverton transect area, north eastern Yilgarn*. Geoscience Australia, pp. 13–35.

Champion D. C. and Cassidy K. F. (2007) *An overview of the Yilgarn Craton and its crustal evolution*. Geoscience Australia, pp. 13–35.

Champion D. C. and Huston D. L. (2016) Radiogenic isotopes, ore deposits and metallogenic terranes: Novel approaches based on regional isotopic maps and the mineral systems concept. *Ore Geol. Rev.* **76**, 229–256.

Champion D. C. and Sheraton J. W. (1997) Geochemistry and Nd isotope systematics of Archaean granites of the Eastern Goldfields, Yilgarn Craton, Australia: implications for crustal growth processes. *Precambrian Res.* **83**, 109–132.

Champion D. C., Budd A. R., Hazell M. S. and Sedgmen A. (2007) *OZCHEM National Whole Rock Geochemistry Dataset*. Geoscience Australia, Canberra.

Collins W. J., Beams S. D., White A. J. R. and Chappell B. W. (1982) Nature and origin of A-type granites with particular reference to Southeastern Australia. *Contrib. Mineral. Petrol.* **80**, 189–200.

Cox K. G., Bell J. D. and Pankhurst R. J. (1979) *The interpretation of igneous rocks*. Springer, Dordrecht, p. 450 pp..

Cumming G. L. and Richards J. R. (1975) Ore lead isotope ratios in a continuously changing earth. *Earth Planet. Sci. Lett.* **28**, 155–171.

Czarnota K., Champion D. C., Goscombe B., Blewett R. S., Cassidy K. F., Henson P. A. and Groenewald P. B. (2010) Geodynamics of the eastern Yilgarn Craton. *Precambrian Res.* **183**, 175–202.

Delavault H., Dhuime B., Hawkesworth C. and Marschall H. R. (2018) Laser-ablation MC-ICP-MS lead isotope microanalysis down to 10 μm: application to K-feldspar inclusions within zircon. *J. Anal. At. Spectrom.* **33**, 195–204.

Doe B. R. and Stacey J. S. (1974) The application of lead isotopes to the problems of ore genesis and ore prospect evaluation: a review. *Econ. Geol.* **69**, 757–776.

Doe B. R. and Zartman R. E. (1979) Plumbotectonics, The Phanerozoic. In *Geochemistry of Hydrothermal Ore Deposits* (ed. H. L. Barnes), 2nd Edition. John Wiley & Sons, New York, pp. 22–70.

Dunphy J. M., Fletcher I. R., Cassidy K. F. and Champion D. C. (2003) *Compilation of SHRIMP U-Pb geochronological data, Yilgarn Craton, Western Australia, 2001-2002* 139 p. Geoscience Australia.

Fletcher I. R. and McNaughton N. J. (2001) Granitoid geochronology: SHRIMP zircon and titanite data MERIWA Report 222, 6.1-6.158. In *Characterisation and Metallogenic Significance of Archean Granitoids of the Yilgarn Craton, Western Australia (AMIRA Project P482/MERIWA Project M281)* (eds. D. C. Champion and K. F. Cassidy). Minerals and Energy Research Institute of Western Australia (MERIWA), Perth, WA, Australia.

Frost B. R. and Frost C. D. (2008) A geochemical classification for feldspathic igneous rocks. *J. Petrol.* **49**, 1955–1969.

Frost B. R., Barnes C. G., Collins W. J., Arculus R. J., Ellis D. J. and Frost C. D. (2001) A geochemical classification for granitic rocks. *J. Petrol.* **42**, 2033–2048.

Frost C. D. and Frost B. R. (1997) Reduced rapakivi-type granites: The tholeiite connection. *Geology* **25**, 647–650.

Gancarz A. J. and Wasserburg G. J. (1977) Initial Pb of the Amîtsoq gneiss, West Greenland, and implications for the age of the Earth. *Geochim. Cosmochim. Acta* **41**, 1283–1301.

Gariépy C. and Allègre C. J. (1985) The lead isotope geochemistry and geochronology of late-kinematic intrusives from the Abitibi greenstone belt, and the implications for late Archaean crustal evolution. *Geochim. Cosmochim. Acta* **49**, 2371–2383.

Gariépy C., Verner D. and Doig R. (1990) Dating Archean metamorphic minerals southeast of the Grenville front, western Quebec, using Pb isotopes. *Geology* **18**, 1078–1081.

Goleby B. R., Blewett R. S., Fomin T., Fishwick S., Reading A. M., Henson P. A., Kennett B. L. N., Champion D. C., Jones L., Drummond B. J. and Nicoll M. (2006) An integrated multi-scale 3D seismic model of the Archaean Yilgarn Craton, Australia. *Tectonophysics* **420**, 75–90.

Goscombe B., Blewett R. S., Czarnota K., Groenewald P. B. and Maas R. (2009) *Metamorphic Evolution and Integrated Terrane Analysis of the Eastern Yilgarn Craton: Rationale, Methods, Outcomes and Interpretation*. Geoscience Australia, 270 pp.

Groves D. I. and Batt W. D. (1984) Spatial and temporal variations of Archaean metallogenic associations in terms of evolution of granitoid-greenstone terrains with particular emphasis on the Western Australian Shield. In *Archaean Geochemistry: The Origin and Evolution of the Archaean Continental Crust* (eds. A. Kröner, G. N. Hanson and A. M. Goodwin). Springer-Verlag, Berlin, pp. 73–98.

Groves D. I., Barley M. E. and Ho S. E. (1989) Nature, genesis, and tectonic setting of mesothermal gold mineralization in the Yilgarn Block, Western Australia. In *The Geology of Gold Deposits: The Perspective in 1988* (eds. R. R. Keays, W. R. H. Ramsay and D. I. Groves). Economic Geology Monograph, pp. 71–85.

Halla J. (2005) Late Archean high-Mg granitoids (sanukitoids) in the southern Karelian domain, eastern Finland: Pb and Nd isotopic constraints on crust-mantle interactions. *Lithos* **79**, 161–178.

Halla J. (2014) Recycling of Lead at Neoarchean Continental Margins. In *Evolution of Archean Crust and Early Life. Modern Approaches in Solid Earth Sciences*, vol. 7 (eds. Y. Dilek and H. Furnes). Springer Netherlands, Dodrecht, pp. 195–213.

Halla J. (2018) Pb isotopes - A multi-function tool for assessing tectonothermal events and crust-mantle recycling at late Archaean convergent margins. *Lithos* **320–321**, 207–221.

Harrison T. M., Baldwin S. L., Caffee M., Gehrels G. E., Schoene B., Shuster D. L. and Singer B. S. (2015) *It's About Time: Opportunities and Challenges for U.S. Geochronology. Institute of Geophysics and Planetary Physics Publication 6539*. University of California, Los Angeles, 56 pp.

Heier K. (1962) Trace elements in feldspars - a review. *Nor. J. Geol.* **42**, 415–454.

Hiess J., Condon D. J., McLean N. and Noble S. R. (2012) $^{238}U/^{235}U$ systematics in terrestrial uranium-bearing minerals. *Science* **335**, 1610–1614.

Hofmann A. W. (1997) Mantle geochemistry: the message from oceanic volcanism. *Nature* **385**, 219–229.

Hollocher K. and Ruiz J. (1995) Major and trace element determinations on NIST glass standard reference materials 611, 612, 614 and 1834 by inductively coupled plasma-mass spectrometry. *Geostandard. Newslett.* **19**, 27–34.

Holmes A. (1946) An estimate of the age of the earth. *Nature* **157**, 680–684.

Houtermans F. G. (1946) Die Isotopenhäufigkeiten im natürlichen Blei und das Alter des Urans. *Naturwissenschaften* **33**(185–186), 219.

Huston D. L., Champion D. C. and Cassidy K. F. (2005) Tectonic controls on the endowment of Archean cratons in VHMS deposits: Evidence from Pb and Nd isotopes. In *Mineral Deposit Research: Meeting the Global Challenge* (eds. J. Mao and F. P. Bierlein). Springer, Berlin, Heidelberg, pp. 15–18.

Huston D. L., Champion D. C. and Cassidy K. F. (2014) Tectonic controls on the endowment of the neoarchean cratons in volcanic-hosted massive sulfide deposits: Evidence from lead and neodymium isotopes. *Econ. Geol.* **109**, 11–26.

Jaffey A. H., Flynn K. F., Glendenin L. E., Bentley W. C. and Essling A. M. (1971) Precision measurement of half-lives and specific activities of ^{235}U and ^{238}U. *Phys. Rev. C* **4**, 1889–1906.

Johnson T. E., Brown M., Gardiner N. J., Kirkland C. L. and Smithies R. H. (2017) Earth's first stable continents did not form by subduction. *Nature* **543**, 239–242.

Jones S. A., Cassidy K. F. and Davis B. K. (2021) Unravelling the D_1 event: evidence for early granite-up, greenstone-down tectonics in the Eastern Goldfields, Western Australia. *Australian J. Earth Sci.* **68**, 1–35.

Koeppel V. and Gruenenfelder M. (1979) Isotope geochemistry of lead. In *Lectures in Isotope Geology* (eds. E. Jager and J. C. Hunziker). Springer Verlag, Berlin, Heidelberg, pp. 134–153.

Korsch R. J., Blewett R. S., Wyche S., Zibra I., Ivanic T. J., Doublier M. P., Romano S. S., Pawley M., Johnson S. P., Van Kranendonk M. J., Jones L. E. A., Kositcin N., Gessner K., Hall C. E., Chen S. F., Patison N., Kennett B. L. N., Jones T., Goodwin J. A., Milligan P. and Costelloe R. D. (2013) *Geodynamic implications of the Youanmi and Southern Carnarvon deep seismic reflection surveys: a ~1300 km traverse from the Pinjarra Orogen to the eastern Yilgarn Craton*. Geological Survey of Western Australia, pp. 147–166.

Kramers J. D. and Tolstikhin I. N. (1997) Two terrestrial lead isotope paradoxes, forward transport modelling, core formation and the history of the continental crust. *Chem. Geol.* **139**, 75–110.

Kumari S., Paul D. and Stracke A. (2016) Open system models of isotopic evolution in Earth's silicate reservoirs: Implications for crustal growth and mantle heterogeneity. *Geochim. Cosmochim. Acta* **195**, 142–157.

Livermore B. D., Connelly J. N., Moynier F. and Bizzarro M. (2018) Evaluating the robustness of a consens $^{238}U/^{235}U$ value for U-Pb geochronology. *Geochim. Cosmochim. Acta* **237**, 171–183.

Ludwig K. R. (2012) User's Manual for Isoplot/Excel 3.75. A Geochronological Toolkit for Microsoft Excel. *Berkeley Geochronol. Center Special Publ.* **5**, 1–75.

Maltese A. and Mezger K. (2020) The Pb isotope evolution of Bulk Silicate Earth: Constraints from its accretion and early differentiation history. *Geochim. Cosmochim. Acta* **271**, 179–193.

McNaughton N. J. and Groves D. I. (1996) A review of Pb-isotope constraints on the genesis of lode-gold deposits in the Yilgarn Craton, Western Australia. *J. R. Soc. West. Aust.* **79**, 123–129.

Miller C. F., Wooden J. F., Bennett V. C., Wright J. E., Solomon G. C. and Hurst R. W. (1990) *Petrogenesis of the composite peraluminous-metaluminous Old Woman-Piute Range batholith, southeastern California; isotopic constraints*. Mem. Geol. Soc. Am., pp. 99–109.

Milot J., Blichert-Toft J., Ayarzagüena S. M., Fetter N., Télouk P. and Albarède F. (2021) The significance of galena Pb model ages and the formation of large Pb-Zn sedimentary deposits. *Chem. Geol.* **583** 120444.

Miyashiro A. (1974) Volcanic rock series in island arcs and active continental margins. *Am. J. Sci.* **274**, 321–355.

Mole D. R., Fiorentini M. L., Thebaud N., McCuaig T. C., Cassidy K. F., Kirkland C. L., Wingate M. T. D., Romano S. S., Doublier M. P. and Belousova E. A. (2012) Spatio-temporal constraints in lithospheric development in the southwest-central Yilgarn Craton, Western Australia. *Aust. J. Earth Sci.* **59**, 625–656.

Mole D. R., Fiorentini M. L., Cassidy K. F., Kirkland C. L., Thebaud N., McCuaig T. C., Doublier M. P., Duuring P., Romano S. S., Maas R., Belousova E. A., Barnes S. J. and Miller J. (2013) Crustal evolution, intra-cratonic architecture and the metallogeny of an Archaean craton. In *Ore Deposits in an Evolving Earth* (eds. G. R. T. Jenkin, P. A. J. Lusty, I. McDonald, M. P. Smith, A. J. Boyce and J. J. Wilkinson). Geol. Soc. London Spec. Publ., pp. 23–80.

Mole D. R., Fiorentini M. L., Thebaud N., Cassidy K. F., McCuaig T. C., Kirkland C. L., Romano S. S., Doublier M. P., Belousova E. A., Barnes S. J. and Miller J. (2014) Archean komatiite volcanism controlled by the evolution of early continents. *Proc. Natl. Acad. Sci. U. S. A.* **111**, 100083–110088.

Mole D. R., Kirkland C. L., Fiorentini M. L., Barnes S. J., Cassidy K. F., Isaac C., Belousova E. A., Hartnady M. and Thebaud N. (2019) Time-space evolution of an Archean craton: A Hf-isotope window into continent formation. *Earth-Sci. Rev.* **196**.

Morris P. A. and Kirkland C. L. (2014) Melting of a subduction-modified mantle source: A case study from the Archean Marda Volcanic Complex, central Yilgarn Craton, Western Australia. *Lithos* **190–191**, 403–419.

Myers J. S. (1995) *The generation and assembly of an Archaean supercontinent: evidence from the Yilgarn Craton, Western Australia*. Geol. Soc. London Spec. Publ., pp. 143–154.

Nesbitt H. W. and Young G. M. (1982) Early Proterozoic climates and plate motions inferred from major element chemistry of lutites. *Nature* **299**, 715–717.

Nutman A. P., Kinny P. D., Compston W. and Williams I. S. (1991) SHRIMP U-Pb zircon geochronology of the Narryer Gneiss Complex, Western Australia. *Precambrian Res.* **52**, 275–300.

Oversby V. M. (1974) New look at the lead isotope growth curve. *Nature* **248**, 132–133.

Paton C., Hellstrom J., Paul B., Woodhead J. and Hergt J. (2011) Iolite: Freeware for the visualisation and processing of mass spectromic data. *J. Anal. At. Spec.* **26**, 2508–2518.

Pawley M. J., Wingate M. T. D., Kirkland C. L., Wyche S., Hall C. E., Romano S. S. and Doublier M. P. (2012) Adding pieces to the puzzle: episodic crustal growth and a new terrane in the northeast Yilgarn Craton, Western Australia. *Aust. J. Earth Sci.* **59**, 603–623.

Pearce N. J. G., Perkins W. T., Westgate J. A., Gorton M. P., Jackson S. E., Neal C. R. and Chenery S. P. (1997) A compilation of new and published major and trace element data fo NIST SRM 610 and NIST SRM 612 glass reference materials. *Geostandard. Newslett.* **21**, 115–144.

Perring C. S. and McNaughton N. J. (1992) The relationship between Archaean gold mineralization and spatially associated minor intrusions at the Kambalda and Norseman gold camps, Western Australia: Lead isotope evidence. *Miner. Depos.* **27**, 10–22.

Schaltegger U., Schmitt A. K. and Horstwood M. S. A. (2015) U-Th-Pb zircon geochronology by ID-TIMS, SIMS, and laser ablation ICP-MS: Recipes, interpretations, and opportunities. *Chem. Geol.* **402**, 89–110.

Schoene B. (2014) U-Th-Pb Geochronology. In *Treatise on Geochemistry* (eds. H. D. Holland and K. K. Turekian), second ed. Elsevier, Oxford, pp. 341–378.

Squire R. J., Allen C. M., Cas R. A. F., Campbell I. H., Blewett R. S. and Nemchin A. A. (2010) Two cycles of voluminous pyroclastic volcanism and sedimentation related to episodic granite emplacement during the late Archean: Eastern Yilgarn Craton, Western Australia. *Precambrian Res.* **183**, 251–274.

Stacey J. S. and Kramers J. D. (1975) Approximation of terrestrial lead isotope evolution by a two-stage model. *Earth Planet. Sci. Lett.* **26**, 207–221.

Stacey J. S., Delevaux M. E. and Ulrych T. J. (1969) Some triple-filament lead isotope ratio measurements and an absolute growth curve for single-stage leads. *Earth Planet. Sci. Lett.* **6**, 15–25.

Steiger R. H. and Jaeger E. (1977) Subcommission on geochronology: Convention on the use of decay constants in geo- and cosmochronology. *Earth Planet. Sci. Lett.* **36**, 359–362.

Storey C. D., Jeffries T. E. and Smith M. (2006) Common lead-corrected laser ablation ICP-MS U-Pb systematics and geochronology of titanite. *Chem. Geol.* **227**, 37–52.

Swager C. P., Witt W. K., Griffin T. J., Ahmat A. L., Hunter W. M., McGoldrick P. J. and Wyche S. (1992) Late Archaean granite-greenstones of the Kalgoorlie Terrane, Yilgarn Craton, Western Australia. In *The Archaean: Terrains, Processes and Metallogeny*, 22 (eds. J. S. Glover and S. E. Ho). University of Western Australia, Geology Department (Key Centre) & University Extension, Publication, pp. 107–122.

Swager C. P., Goleby B. R., Drummond B. J., Rattenbury M. S. and Williams P. R. (1997) Crustal structure of granite-greenstone terranes in the Eastern Goldfields, Yilgarn Craton, as revealed by seismic reflection profiling. *Precambrian Res.* **83**, 43–56.

Tessalina S. G., Herrington R. J., Taylor R. N., Sundblad K., Maslennikov V. V. and Orgeval J.-J. (2016) Lead isotopic systematics of massive sulphide deposits in the Urals: Applications for geodynamic setting and metal sources. *Ore Geol. Rev.* **72**, 22–36.

Tyrrell S., Haughton P. D. W., Daly J. S., Kokfelt T. F. and Gagnevin D. (2006) The use of the common Pb isotope composition of detrital K-Feldspar grains as a provenance tool

and its application to Upper Carboniferous paleodrainage, Northern England. *J. Sediment. Res.* **76**, 324–345.

Tyrrell S., Haughton P. D. W., Daly J. S. and Shannon P. M. (2012) The Pb isotopic composition of detrital K-feldspar: A tool for constraining provenance, sedimentary processes and paleodrainage. In *Quantitative Mineralogy and Microanalysis of Sediments and Sedimentary Rocks*, Vol. 42 (ed. P. Sylvester). Mineralogical Association of Canada Short Course Series, pp. 203–217.

Van Kranendonk M. J., Smithies R. H., Hickman A. H. and Champion D. C. (2007) Review: secular tectonic evolution of Archean continental crust: interplay between horizontal and vertical processes in the formation of the Pilbara Craton, Australia. *Terra Nova* **19**, 1–38.

Van Kranendonk M. J., Ivanic T. J., Wingate M. T. D., Kirkland C. L. and Wyche S. (2013) Long-lived autochthonous development of the Archean Murchison Domain, and implications for Yilgarn Craton tectonics. *Precambrian Res.* **229**, 49–92.

Wareham C. D., Pankhurst R. J., Thomas R. J., Storey B. C., Grantham G. H., Jacobs J. and Eglington B. M. (1998) Pb, Nd and Sr isotope mapping of grenville-age crustal provinces in Rodinia. *J. Geol.* **106**, 647–660.

Wooden J. L., Kistler R. W. and Tosdal R. M. (1998) Pb isotopic mapping of crustal structure in the northern Great Basin and relationships to Au deposit trends. In *Contributions to the Gold Metallogeny of Northern Nevada, United States Geological Survey Open-File Report* (ed. R. M. Tosdal). pp. 20–33.

Wyche N. L. and Wyche S. (2017) Yilgarn Craton Geology. In *Australian Ore Deposits*, Monograph 32 (ed. G. N. Phillips). The Australasian Institute of Mining and Metallurgy, Melbourne, pp. 89–94.

Wyche S., Kirkland C. L., Riganti A., Pawley M. J., Belousova E. and Wingate M. T. D. (2012) Isotopic constraints on stratigraphy in the central and eastern Yilgarn Craton, Western Australia. *Aust. J. Earth Sci.* **59**, 657–670.

Wyche S., Ivanic T. J. and Zibra, I. (compilers) (2013) Youanmi and Southern Carnarvon seismic and magnetotelluric (MT) workshop 2013. Geological Survey of Western Australia, Record 2013/6, 180 pp.

Wyche S., Lu Y. and Wingate M. T. D. (2019) Evidence of Hadean to Paleoarchean Crust in the Youanmi and South West Terranes, and Eastern Goldfields Superterrane of the Yilgarn Craton, Western Australia. In *Earth's Oldest Rocks, Second Edition* (eds. M. J. Van Kranendonk, V. C. Bennett and J. E. Hoffmann). pp. 279–292.

Zartman R. E. (1974) Lead isotopic provinces in the Cordillera of the western United States and their geologic significance. *Econ. Geol.* **69**, 792–805.

Zartman R. E. and Doe B. R. (1981) Plumbotectonics-the model. *Tectonophysics* **75**, 135–162.

Zartman R. E. and Haines S. M. (1988) The plumbotectonic model for Pb isotopic systematics among major terrestrial reservoirs – A case for bi-directional transport. *Geochim. Cosmochim. Acta* **52**, 1327–1339.

Zartman R. E. and Wasserburg G. J. (1969) The isotopic composition of lead in potassium feldspars from some 1.0-b.y. old North American igneous rocks. *Geochim. Cosmochim. Acta* **33**, 901–942.

Zhang Z., Tyrrell S., Li C., Daly J. S., Sun X. and Li Q. (2014) Pb isotope compositions of detrital K-feldspar grains in the upper-middle Yangtze River system: Implications for sediment provenance and drainage evolution. *Geochem. Geophys.* **15**, 2765–2779.

Associate editor: Janne Blichert-Toft